Mesoscopic modeling of random walk and reactions in crowded media

Stefan Engblom[*] and Per Lötstedt[†]
Division of Scientific Computing, Department of Information Technology, Uppsala University, SE-751 05 Uppsala, Sweden

Lina Meinecke[‡]
Department of Mathematics, University of California, Irvine, California 92697-3875, USA

(Received 1 March 2018; published 11 September 2018)

We develop a mesoscopic modeling framework for diffusion in a crowded environment, particularly targeting applications in the modeling of living cells. Through homogenization techniques we effectively coarse grain a detailed microscopic description into a previously developed internal state diffusive framework. The observables in the mesoscopic model correspond to solutions of macroscopic partial differential equations driven by stochastically varying diffusion fields in space and time. Analytical solutions and numerical experiments illustrate the framework.

DOI: 10.1103/PhysRevE.98.033304

I. INTRODUCTION

Living cells are controlled by a complicated network of reaction-diffusion events. An example is exogenous signals triggering the cell's response by reacting with the proteins present in the cell or binding to the DNA to initiate transcription of certain genes. An important task in computational systems biology is to study these processes as accurately as possible inside the complicated cell geometry. We specifically target two special features in a model of the biochemical processes in living cells in this article: *the high percentage of occupied volume in the cytoplasm* and *the intrinsic noise*.

It is estimated that up to 40% of the available space in the cytoplasm is occupied by macromolecules [1,2] and these have been shown to alter the dynamics of the reaction network [3] (see also Fig. 1). Due to the multiple steric repulsions between the tracer molecules and the crowders, diffusion is slowed down. This macromolecular crowding effect plays an even more important role on the cell membrane [4], where actin filaments create barriers for the motion of membrane bound proteins [5–7].

New imaging techniques [8] have shown that the slowdown happens gradually over time. The tracers initially diffuse freely without encountering the crowding macromolecules. Then, they start colliding with the crowders and go through an anomalous phase of diffusion where their movement is constantly slowed down and their mean-square displacement (MSD) therefore grows sublinearly with time [9–12]. Let $\langle\cdot\rangle$ denote the average over the sample trajectories of the molecules and let $\|\mathbf{x}\|_2$ be the Euclidean length of a coordinate vector $\mathbf{x}$. The MSD of a molecule at $\mathbf{x}(t)$ at time t released at $\mathbf{x}(0) = 0$ at $t = 0$ behaves as

$$\left\langle \left\| \mathbf{x}(t) \right\|_2^2 \right\rangle \propto t^{\alpha}, \tag{1}$$

where $\alpha = 1$ for ordinary diffusion and $\alpha \in (0, 1)$ in subdiffusion where, at least in a time interval shortly after $t = 0$, the molecules diffuse anomalously (see [11]). On a long time scale they can be observed to be diffusing normally again, but at a reduced diffusion constant compared to the tracer in a dilute medium. This change in diffusivity is a hydrodynamic consequence of the highly crowded space inside cells. Moreover, the crowders also exhibit a thermodynamic effect on the chemical reactions [13], which can be both impeded (due to the longer time until collision) or facilitated (due to the smaller effective reaction volume). In this paper, we will only investigate inert crowders and their effect due to steric repulsion with the reacting molecules. More complicated interactions such as transient binding or interaction potentials further impact the reaction-diffusion dynamics in a crowded environment [14–17], but lie outside the scope of this study.

The second feature we incorporate in our modeling framework is stochasticity. Although the cytosol is densely packed with molecules, the individual species is often present at low copy numbers. A deterministic macroscopic model describing the mean value of the concentrations of the chemical species is therefore not applicable and stochastic models remain as the computationally feasible alternative [18–22]. On a mesoscopic or on-lattice level of modeling, the domain is partitioned into voxels and diffusion is modeled as a random jump process of the molecules between the voxels. Inside each voxel, space is not resolved further and the molecules are assumed to be well mixed and react randomly with other molecules located within the same voxel. The time evolution of this system is described by the reaction-diffusion master equation [23]. We sample trajectories of the system using stochastic simulation techniques as popularized by Gillespie [24], originally developed for well stirred problems without

[*]stefane@it.uu.se
[†]perl@it.uu.se
[‡]lina.meinecke@uci.edu

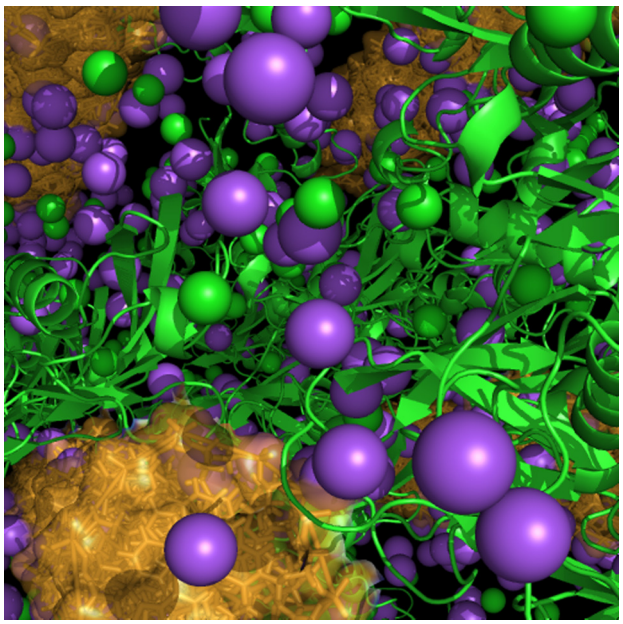

FIG. 1. A snapshot from a molecular dynamics simulation: the interior of an *E. coli* is a highly crowded environment. Picture courtesy of David van der Spoel, Uppsala University.

spatial dependence. Discretizations of spatial domains were first considered in [25–27] and later improved to allow for unstructured meshes in [28,29]. Overviews of deterministic, macroscopic and stochastic, mesoscopic and microscopic levels of modeling of biochemical networks are found in, e.g., [30–33].

There have been several models combining the macromolecular crowding effects and the stochastic mesoscopic level. In [34] the most highly crowded voxels are defined as full and are made inaccessible for the tracer molecules in order to model crowding. A more gradual approach is to define the number of possible molecules per voxel and then rescale the propensity to jump into this voxel by how many spots are already occupied by other molecules [35–37]. But, by averaging the effect of the crowders over the whole voxel, the transient anomalous phase is not captured and we only observe the long-time slower diffusion. To resolve the short-time microscopic information, the positions of stationary obstacles were homogenized (or coarse grained, upscaled) to mesoscopic jump rates in [38]. The crowders can have arbitrary shape, but the diffusing tracers are understood to be circular in two space dimensions (2D) and spherical in three dimensions (3D).

In Brownian dynamics (BD) each individual molecule is tracked in a lattice-free (or off-lattice) microscopic model. Here, all molecules are spherical, move in Brownian motion, and react with a certain probability when they touch each other [39,40]. Crowding is automatically incorporated in the model by the excluded volume of the stationary or moving crowders. A stochastic, microscopic simulation is in general more accurate than a mesoscopic simulation but also much more computationally expensive. Microscopic simulation of crowding and diffusion at the particle level is proposed in [41] and is evaluated in [12,42]. In [43] off-grid microscopic simulations are compared to grid based microscopic cellular automata simulations and the grid artifacts are quantified.

On the deterministic, macroscopic level, anomalous diffusion of the concentrations due to crowding can be modeled by fractional partial differential equations (FPDEs) [11,44,45]. Internal states are introduced in [46] on the mesoscopic level to model anomalous diffusion and in [47] for reactions. The internal state of a molecule changes with a certain probability and determines the molecule's diffusion speed. The intensities for these changes are given by the macroscopic FPDE for the observed variables in [46,47]. Memory effects are included without sacrificing the Markov property using these internal states. Three physical interpretations of these internal states are that the molecule is in different geometrical conformations, has different methylation or phosphorylation, or resides in differently crowded environments, which are all affecting the diffusion speed and reaction propensities. Hidden states are also introduced in [48] to explain data from single cell experiments.

In this paper, we will combine the internal states model derived in [47] with the multiscale approach in [38] to efficiently model diffusion of tracer particles among stationary or moving crowder obstacles. The method

(1) is considerably faster than Brownian dynamics,

(2) allows more versatile modeling than mesoscopic methods where a limited number of molecules can occupy a lattice node,

(3) defines a random diffusion field for a macroscopic equation expressed in observables.

We first coarse grain the microscale to the mesoscale by determining statistics for the variation in the diffusion coefficient with the homogenization method in [38]. The parameters of the internal states model in [47] can subsequently be deduced from these data. Our mesoscopic method for crowding is less heuristic than other methods and can be defined by experimental data, e.g., from [48]. The mesoscale equations are coarse grained to the macroscale analytically resulting in partial differential equations (PDEs) for the observables.

In the next section, we first present the two mesoscopic models from [47] and [38] in more detail. We couple the statistics from the microlevel to the parameters in the internal state model in Sec. III. The distributions of the molecules in certain chemical systems with internal states and diffusion are multinomial as shown by the analysis in Sec. IV. In Sec. V, we test the resulting coarse-grained model in examples in 2D and 3D and a summarizing discussion is found in the final section.

II. TWO MESOSCOPIC MODELS

The effect of static crowding molecules is coarse grained from the microscopic to the mesoscopic level of approximation according to [38]. Then, a discretized mesoscopic model built from an internal states approximation is reviewed following [46,47]. A differential equation for biochemical networks with diffusion and reactions is discretized in time, space, and the internal state space by the finite element method (FEM). A relation is derived between a mesoscopic system with internal states and a macroscopic equation for the observable variables.

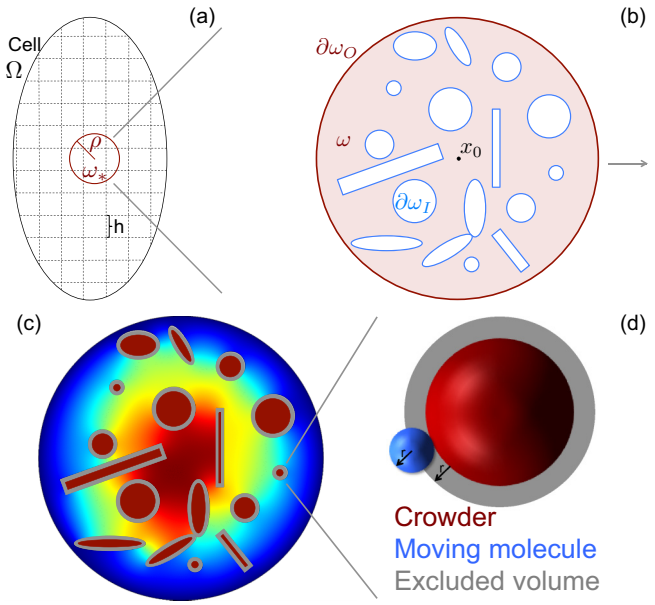

FIG. 2. (a) The cell volume Ω discretized by a grid with size h giving rise to the nonperforated subvolumes ω_*. (b) The circular, perforated domain ω (pink) of radius ρ where the cutouts represent the obstacles, and the outer $\partial\omega_O$ and inner $\partial\omega_I$ boundaries. (c) Solution to (2) on ω with crowders represented as holes with reflective boundary conditions and with high values of $E(\mathbf{x})$ in red (in the middle) and low values in blue (along the outer boundary). (d) The excluded volume consists of the volume occupied by the crowding molecule enlarged by the radius r of the diffusing tracer molecule.

A. Microscopic to mesoscopic model via first exit times

Single tracer molecules move on the microscopic scale by Brownian motion in a domain ω_* with obstacles. The moving molecules are assumed to be circular in 2D and spherical in 3D with radius r. The crowder obstacles are stationary in space and chemically inert, such that the boundary condition for the moving molecule is reflective at the surface of the crowding objects, which are represented explicitly as holes in ω_*. Similar models for crowded media are the Lorentz model in [49] and the cherry-pit model in [50]. The properties of the media are explored by Brownian dynamics in [49,50].

The volume of the interior of the cell is denoted by Ω and is discretized into a Cartesian grid with size h. This grid defines circular (2D) or spherical (3D) subvolumes ω_* with radius $\rho = h$ covering the voxels in the mesoscopic model. The subvolumes ω_* overlap and are occupied by crowders such that the free space remaining for the moving molecule is ω and $\omega \subseteq \omega_*$ [see Figs. 2(a) and 2(b)].

Let γ_0 be the diffusion coefficient for the Brownian motion. In [38] we presented a multiscale approach to compute the effective diffusion rate γ in the crowded environment ω_* using the mean value of the first exit time $E(\mathbf{x})$ (see [51]) from ω fulfilling

$$\gamma_0 \Delta E(\mathbf{x}) = -1, \quad \mathbf{x} \in \omega \tag{2}$$

$$E(\mathbf{x}) = 0, \quad \mathbf{x} \in \partial\omega_O \tag{3}$$

$$\mathbf{n} \cdot \nabla E(\mathbf{x}) = 0, \quad \mathbf{x} \in \partial\omega_I. \tag{4}$$

The starting position of the diffusing molecule is $\mathbf{x} \in \omega$, $\partial\omega_O$ is the outer boundary of ω shared with ω_*, and $\partial\omega_I$ is the inner boundary of the obstacles with normal $\mathbf{n}$ [see Fig. 2(b)]. Since (2) describes the expected exit time of a moving point particle, the cutouts in the perforated domain are enlarged to account for the radius r of the tracer [see Fig. 2(d)].

Equation (2) and boundary condition (3) also hold on the nonperforated domain ω_* without the boundary condition on $\partial\omega_I$ and resulting in the solution $E_*(\mathbf{x})$. In dilute media without any crowders, the first exit time can be used to recover the jump rates on a Cartesian mesh [see Fig. 2(a)], by evaluating $E(\mathbf{x})$ in the center of the circle $\mathbf{x}_0$. Since the first exit time approach for mesoscopic diffusion in a crowded environment has to converge to the well defined dilute rates on a Cartesian mesh for $\phi \to 0$, where $\phi \in [0, 1]$ is the percentage of occupied volume, we evaluate E in the center. The mean first exit time in (2) is inversely proportional to the diffusion coefficient and we can compute the effective diffusion rate γ in the crowded domain ω_* according to

$$\gamma = \gamma_0 \frac{E_*(\mathbf{x}_0)}{E(\mathbf{x}_0)}. \tag{5}$$

In this way, all the details in ω are avoided and an effective (or homogenized, upscaled, coarse-grained) diffusion coefficient γ in ω_* is determined. The effective diffusion rate γ depends on $\phi \in [0, 1]$. If $\phi = 0$, then $E_*(\mathbf{x}) = E(\mathbf{x})$ and $\gamma = \gamma_0$ in (5) and if $\phi \to 1$, then there is no space left for molecular motion, $E(\mathbf{x}) \to \infty$, and $\gamma \to 0$. Depending on the shape of the obstacles and the size of the moving molecule r, γ can be 0 for a small $\phi < 1$.

This approach is universal in the way that the stationary crowding molecules can have any shape. If the crowders are spherical with radius R, the radii have to satisfy $r, R \ll \rho$ for the upscaling to be accurate and not too sensitive to the particular distribution of the obstacles. New γ values for other shapes are determined in [38]. The typical size of a moving or crowding molecule is 4–20 nm (globular protein-ribosome). Then, a possible ρ is $\rho \sim 50$ nm, which is sufficiently small to discretize a prokaryote *E. coli* of size 1–3 μm or a eukaryotic cell which is about 10 times larger.

B. Internal states model

The mesoscopic model for diffusion and chemical reactions is extended such that each molecule can adopt several internal states that may be unobservable. These extra internal states are used to model subdiffusion in [46,47] and will be used here to represent the varying density of the tracer's environment due to moving obstacles.

The differential equation for the concentration of one chemical species is first derived without reactions. The dynamic change of internal state is achieved by adding an integral term. The equation is discretized by FEM in space and the internal states. The computational mesh in space is structured or unstructured and the internal state space is discretized by an equidistant grid. The equations are then generalized to many species and chemical reactions.

1. Spatial internal states model

Let $u(\mathbf{x}, t, \xi)$ be the concentration of a molecular species at $\mathbf{x} \in \Omega$ at time $t \geqslant 0$ in a continuous internal state $\xi \in \Xi = [0, \xi_{\max}] \subset \mathbb{R}_+$. The rate of change from internal state η to state ξ is $A(\xi, \eta)$. The rate of the chemical reactions depends on the concentration and the internal state in $f(u, \xi)$ but is independent of time and space. At the boundary $\partial\Omega$ of Ω the molecules are reflected and the scalar diffusion $\gamma(\xi)$ is allowed to depend on the internal state. Then, u satisfies, for $t > 0$,

$$u_t(\mathbf{x}, t, \xi) = \nabla \cdot (\gamma(\xi)\nabla u(\mathbf{x}, t, \xi)) + \int_\Xi A(\xi, \eta)u(\mathbf{x}, t, \eta)\, d\eta + f(u, \xi) \quad (6)$$

for $\mathbf{x} \in \Omega,\ \xi \in \Xi$,

$$\mathbf{n} \cdot \nabla u = 0 \quad (7)$$

for $\mathbf{x} \in \partial\Omega,\ \xi \in \Xi$. The subscript t denotes a time derivative.

Let us begin with the equation for the diffusion and change of internal state and ignore the reactions in f. The total amount of the species $\int_\Omega \int_\Xi u(\mathbf{x}, t, \xi)\, d\xi\, d\mathbf{x}$ should remain constant for mass conservation. By integrating (6) over Ξ and Ω using the boundary condition on $\partial\Omega$, we obtain the time derivative

$$\begin{aligned}
\partial_t \int_\Xi \int_\Omega u(\mathbf{x}, t, \xi)\, d\xi\, d\mathbf{x} &= \int_\Xi \int_\Omega \nabla \cdot (\gamma(\xi)\nabla u(\mathbf{x}, t, \xi))\, d\mathbf{x}\, d\xi \\
&\quad + \int_\Xi \int_\Omega \int_\Xi A(\xi, \eta)u(\mathbf{x}, t, \eta)\, d\eta\, d\mathbf{x}\, d\xi \\
&= \int_\Xi \gamma(\xi) \int_{\partial\Omega} \mathbf{n} \cdot \nabla u(\mathbf{x}, t, \xi)\, ds\, d\xi \\
&\quad + \int_\Omega \int_\Xi u(\mathbf{x}, t, \eta) \int_\Xi A(\xi, \eta)\, d\xi\, d\eta\, d\mathbf{x} \\
&= \int_\Omega \int_\Xi u(\mathbf{x}, t, \eta) \int_\Xi A(\xi, \eta)\, d\xi\, d\eta\, d\mathbf{x}. \quad (8)
\end{aligned}$$

The time derivative of the total amount must vanish for all u. Thus, a sufficient condition on A for this to hold is

$$\int_\Xi A(\xi, \eta)\, d\xi = 0. \quad (9)$$

The observable $U(\mathbf{x}, t)$ denotes the concentration of the molecule independent of its internal state and is defined by

$$U(\mathbf{x}, t) = \int_\Xi u(\mathbf{x}, t, \xi)\, d\xi. \quad (10)$$

If A is chosen as in (9) then by (6), U in (10) satisfies

$$U_t(\mathbf{x}, t) = \nabla \cdot \int_\Xi \gamma(\xi)\nabla u(\mathbf{x}, t, \xi)\, d\xi. \quad (11)$$

There is an ordinary diffusion equation for U only if γ is independent of ξ. With a diffusion tensor $\tilde{\gamma}_i(\mathbf{x}, t),\ i = 1, \ldots, d$, such that

$$\tilde{\gamma}_i(\mathbf{x}, t) = \int_\Xi \gamma(\xi)\partial_{x_i} u(\mathbf{x}, t, \xi)\, d\xi / \partial_{x_i} \int_\Xi u(\mathbf{x}, t, \xi)\, d\xi,$$

(11) can be written

$$U_t = \nabla \cdot (\tilde{\boldsymbol{\gamma}}(\mathbf{x}, t)\nabla U), \quad (12)$$

but in general $\tilde{\boldsymbol{\gamma}}$ is not known explicitly.

A particular choice of A is

$$A(\xi, \eta) = [\mu(\xi) - \delta(\xi - \eta)]T(\eta) \quad (13)$$

with the Dirac measure δ. Then, (9) is fulfilled if μ is scaled such that

$$\int_\Xi \mu(\xi)\, d\xi = 1. \quad (14)$$

In order to find the steady state solution of (6), we set tentatively

$$u_\infty(\xi) = \mu(\xi)/T(\xi). \quad (15)$$

Clearly,

$$\int_\Xi A(\xi, \eta)u_\infty(\eta)\, d\eta = 0, \quad (16)$$

and u_∞ is indeed a steady state solution of (6). A natural convention is to let $\mu(\xi) \geqslant 0$ and $T(\xi) > 0$ for u_∞ to be a non-negative concentration.

2. Discretization in space and internal states

Let Ω be discretized by a triangular (2D) or tetrahedral (3D) primal mesh with nodes at $\mathbf{x}_i,\ i = 1, \ldots, J$. The dual mesh consists of voxels $\mathcal{V}_i,\ i = 1, \ldots, J$, as in [29]. Each node $\mathbf{x}_i$ is associated with one voxel $\mathcal{V}_i$. The solution u of (6) is approximated by the finite element method using linear basis functions $\varphi_i(\mathbf{x})$ satisfying $\varphi_i(\mathbf{x}_i) = 1$ and $\varphi_i(\mathbf{x}_j) = 0,\ j \neq i$. The internal state space Ξ is partitioned into K intervals $\mathcal{I}_k = [\xi_{k-1}, \xi_k],\ k = 1, \ldots, K$, of length $\Delta\xi = \xi_{\max}/K$. In each interval k there is a basis function ψ_k such that $\psi_k(\xi) = 1/\sqrt{\Delta\xi},\ \xi \in \mathcal{I}_k$, and $\psi_k(\xi) = 0$ otherwise. Then, u_h approximating u is

$$u_h(\mathbf{x}, t, \xi) = \sum_{j=1}^{J} \sum_{l=1}^{K} u_{jl}(t)\varphi_j(\mathbf{x})\psi_l(\xi). \quad (17)$$

Insert u_h into (6), multiply by a test function $\varphi_i(\mathbf{x})\psi_k(\xi)$ in a tensor product finite element space, and integrate over $\Omega \times \Xi$ to derive an equation for the evolution of u_{jl}. If ξ in (6) is interpreted as a random variable determining the diffusion, then (17) is the approximation suitable for a stochastic Galerkin method to solve (6) [52].

Let E_α be a triangular element in 2D or a tetrahedral element in 3D with area or volume $|E_\alpha|$ and $\mathcal{T}_{ij}$ the set of triangles or tetrahedra with a common edge ij between nodes i and j. The Kronecker delta is denoted by δ_{ij}. An element in the stiffness tensor S is then

$$\begin{aligned}
S_{ijkl} &= -\sum_{E_\alpha \in \mathcal{T}_{ij}} \int_{E_\alpha} \nabla\varphi_i^T|_{E_\alpha} \nabla\varphi_j|_{E_\alpha}\, d\mathbf{x} \int_\Xi \gamma(\xi)\psi_k(\xi)\psi_l(\xi)\, d\xi \\
&= -\sum_{E_\alpha \in \mathcal{T}_{ij}} \nabla\varphi_i^T|_{E_\alpha} \nabla\varphi_j|_{E_\alpha} |E_\alpha|\gamma_k\delta_{kl} = \gamma_k S_{ij}\delta_{kl}, \quad (18)
\end{aligned}$$

where γ_k is the average of $\gamma(\xi)$ in $\mathcal{I}_k$. In the diagonal element with $i = j$, the integration domain in $\mathbf{x}$ is over all E_α with a corner at $\mathbf{x}_i$. Choose γ_k to be $\gamma_0 T(k)$ and let $\mathbf{T}$ be the matrix

with $T(k)$ in the diagonal. Hence, with a stiffness matrix $\mathbf{S}$ the stiffness tensor in (18) can be written

$$S = \gamma_0 \mathbf{S} \otimes \mathbf{T}, \tag{19}$$

where $\otimes$ denotes the Kronecker product.

The mass tensor $\tilde{M}$ is defined by

$$\begin{aligned}\tilde{M}_{ijkl} &= \sum_{E_\alpha \in \mathcal{T}_{ij}} \int_{E_\alpha} \varphi_i(\mathbf{x})\varphi_j(\mathbf{x})\, d\mathbf{x} \int_{\Xi} \psi_k(\xi)\psi_l(\xi)\, d\xi \\ &= \tilde{M}_{ij}\delta_{kl}. \end{aligned} \tag{20}$$

The first part of $\tilde{\mathbf{M}}$ depends on the geometry and is lumped and replaced by a diagonal matrix $\mathbf{M}$ such that

$$M_{ij} = M_i \delta_{ij}, \quad M_i = \sum_{l=1}^{J} \tilde{M}_{il}. \tag{21}$$

Then, by (20)

$$\tilde{M}_{ijkl} = M_i \delta_{ij}\delta_{kl}. \tag{22}$$

An element in the tensor discretizing the operator A for change of internal state is

$$\begin{aligned} A_{ijkl} = &- \sum_{E_\alpha \in \mathcal{T}_{ij}} \int_{E_\alpha} \varphi_i(\mathbf{x})\varphi_j(\mathbf{x})\, d\mathbf{x} \\ &\times \int_{\Xi\times\Xi} A(\xi,\eta)\psi_k(\xi)\psi_l(\eta)\, d\xi\, d\eta = \kappa_0 \tilde{M}_{ij} A_{kl}, \end{aligned} \tag{23}$$

where A_{kl} is an element in the matrix $\mathbf{A}$ and κ_0 is a freely choosable scaling of $\mathbf{A}$ that denotes how fast the molecules change their internal state. Thus, A can be written as $A = \kappa_0 \mathbf{M} \otimes \mathbf{A}$ after mass lumping of $\tilde{M}$.

Let $\mathbf{e}_J$ be defined by $\mathbf{e}_J^T = (1, 1, \ldots, 1) \in \mathbb{R}^J$ and let $\mu(\xi)$ be a piecewise constant function such that $\mu(\xi) = \sum_{k=1}^{K} \mu_k \psi_k(\xi)$. Then, the matrix-vector forms of the condition in (9), the special choice of A in (13), the scaling of the components of $\boldsymbol{\mu} = (\mu_1, \ldots, \mu_K)^T$ in (14), and the null vector $\mathbf{u}_{i\infty} = (u_{i\infty 1}, \ldots, u_{i\infty K})^T$ of $\mathbf{A}$ in (15) are

$$\begin{aligned} &\mathbf{e}_K^T \mathbf{A} = \mathbf{0}, \ \mathbf{A} = \big(\boldsymbol{\mu}\mathbf{e}_K^T - \mathbf{I}_K\big)\mathbf{T}, \ \mathbf{e}_K^T \boldsymbol{\mu} = 1, \\ &\mathbf{u}_{i\infty} = \mathbf{T}^{-1}\boldsymbol{\mu} \Longrightarrow \mathbf{A}\mathbf{u}_{i\infty} = \mathbf{0}, \end{aligned} \tag{24}$$

where $\mathbf{I}_J$ is the identity matrix of dimension $J \times J$. These properties are shared by $\mathbf{A}$ in [46,47]. Since $\mathbf{e}_K^T \mathbf{A} = \mathbf{0}$, there is one eigenvalue of $\mathbf{A}$ equal to 0 with eigenvector $\mathbf{u}_{i\infty}$. The diagonal elements of $\mathbf{A}$ are negative and it follows from Gerschgorin's theorem that the real parts of the eigenvalues of $\mathbf{A}$ are nonpositive.

The diffusion matrix $\mathbf{D}$ is defined by

$$\mathbf{D} = \gamma_0 \mathbf{M}^{-1}\mathbf{S}. \tag{25}$$

With the expressions derived in (19) and (23) and multiplication by the inverse of the lumped mass matrix, the discretized equation (6) for all concentrations $\mathbf{u}$ is

$$\mathbf{u}_t = \gamma_0(\mathbf{D} \otimes \mathbf{T})\mathbf{u} + \kappa_0(\mathbf{I}_J \otimes \mathbf{A})\mathbf{u}, \tag{26}$$

or for the concentration $\mathbf{u}_i$ in voxel i

$$\mathbf{u}_{it} = \gamma_0 \mathbf{T}\left(\sum_{j\in\mathcal{J}(i)} D_{ij}\mathbf{u}_j + D_{ii}\mathbf{u}_i \right) + \kappa_0 \mathbf{A}\mathbf{u}_i, \ i = 1, \ldots, J. \tag{27}$$

The index set $\mathcal{J}(i)$ consists of the indices j with an edge connecting $\mathbf{x}_i$ and $\mathbf{x}_j$ implying that $D_{ij} \neq 0$. The vector $\mathbf{u} \in \mathbb{R}^{JK}$ has components u_{ik}, $i = 1, 2, \ldots, J$, $k = 1, 2, \ldots, K$, denoting the concentration in the internal state k at node or voxel i and $\mathbf{u}_i$ is a subset of $\mathbf{u}$ restricted to all the internal states in voxel i.

The mean values $\bar{y}_{ik}$ of the copy numbers of the species satisfy (27) with $\mathbf{u}_i = |\mathcal{V}_i|^{-1}\bar{\mathbf{y}}_i$:

$$\begin{aligned} \bar{\mathbf{y}}_{it} &= \gamma_0 \mathbf{T}\left(\sum_{j\in\mathcal{J}(i)} \frac{S_{ij}}{|\mathcal{V}_j|}\bar{\mathbf{y}}_j + \frac{S_{ii}}{|\mathcal{V}_i|}\bar{\mathbf{y}}_i \right) + \kappa_0 \mathbf{A}\bar{\mathbf{y}}_i \\ &= \gamma_0 \mathbf{T}\left(\sum_{j\in\mathcal{J}(i)} \lambda_{ji}\bar{\mathbf{y}}_j - \lambda_i \bar{\mathbf{y}}_i \right) + \kappa_0 \mathbf{A}\bar{\mathbf{y}}_i, \ i = 1, \ldots, J \end{aligned} \tag{28}$$

where λ_{ji}, S_{ij}, and D_{ij} in (27) and (28) are related by

$$\begin{aligned} &\lambda_{ji} = \frac{S_{ij}}{|\mathcal{V}_j|}, \ D_{ij} = \frac{|\mathcal{V}_j|}{|\mathcal{V}_i|}\lambda_{ji}, \\ &\lambda_i = -D_{ii}, \ \sum_{j\in\mathcal{J}(i)} |\mathcal{V}_j|\lambda_{ji} = |\mathcal{V}_i|\lambda_i, \ \sum_{i,i\neq j} \lambda_{ji} = \lambda_j \end{aligned} \tag{29}$$

(see [29]). The vector $\bar{\mathbf{y}}$ holds $\bar{\mathbf{y}}_i$, $i = 1, \ldots, J$, stored consecutively. With $\Lambda_{ij} = \lambda_{ji}$, the equation for $\bar{\mathbf{y}}$ is similar to (26):

$$\bar{\mathbf{y}}_t = \gamma_0(\boldsymbol{\Lambda} \otimes \mathbf{T})\bar{\mathbf{y}} + \kappa_0(\mathbf{I}_J \otimes \mathbf{A})\bar{\mathbf{y}}. \tag{30}$$

The sum of the components in $\bar{\mathbf{y}}$ is

$$\sum_{i=1}^{J}\sum_{k=1}^{K} y_{ik} = (\mathbf{e}_J \otimes \mathbf{e}_K)^T \bar{\mathbf{y}}. \tag{31}$$

By (29) we have $\mathbf{e}_J^T \boldsymbol{\Lambda} = \mathbf{0}$. Hence,

$$\begin{aligned} ((\mathbf{e}_J \otimes \mathbf{e}_K)^T \bar{\mathbf{y}})_t &= (\mathbf{e}_J \otimes \mathbf{e}_K)^T \bar{\mathbf{y}}_t \\ &= \gamma_0\big(\mathbf{e}_J^T \boldsymbol{\Lambda} \otimes \mathbf{e}_K^T \mathbf{T}\big)\bar{\mathbf{y}} \\ &\quad + \kappa_0\big(\mathbf{e}_J^T \mathbf{I}_J \otimes \mathbf{e}_K^T \mathbf{A}\big)\bar{\mathbf{y}} = \mathbf{0}, \end{aligned} \tag{32}$$

since $\mathbf{e}_K^T \mathbf{A} = \mathbf{0}$ in (24). Consequently, the sum in (31) is constant in time:

$$\sum_{i=1}^{J}\sum_{k=1}^{K} y_{ik}(t) = \sum_{i=1}^{J}\sum_{k=1}^{K} y_{ik}(0), \quad t > 0. \tag{33}$$

The jump coefficients $\lambda_{ji} \geqslant 0$ are proportional to the probability of a molecule in voxel $\mathcal{V}_j$ to jump to $\mathcal{V}_i$ in a stochastic simulation of the system [29]. A non-negative λ_{ji} is required for an interpretation of it as a probability. In a mesh of poor quality, λ_{ji} may be negative due to an $S_{ij} < 0$ in the finite element discretization but corrections are derived in [53,54] such that $\lambda_{ji} \geqslant 0$ on any mesh.

It follows from the properties of λ_{ji} in (29) and $\mathbf{A}$ in (24) that there is a stationary solution $\bar{\mathbf{y}}_{i\infty} = v_i \mathbf{T}^{-1}\boldsymbol{\mu}$,

$i = 1, \ldots, J$, with $v_i = |\mathcal{V}_i|$ to (28) such that

$$\bar{\mathbf{y}}_{i\infty t} = \gamma_0 \mathbf{T}\left(\sum_{j\in\mathcal{J}(i)} \lambda_{ji}\bar{\mathbf{y}}_{j\infty} - \lambda_i \bar{\mathbf{y}}_{i\infty}\right) + \kappa_0 \mathbf{A}\bar{\mathbf{y}}_{i\infty} = \mathbf{0}. \quad (34)$$

Hence, with $\bar{\mathbf{y}}_\infty = \bar{y}\mathbf{v} \otimes \mathbf{T}^{-1}\boldsymbol{\mu}$ in (30)

$$\bar{\mathbf{y}}_{\infty t} = \gamma_0 \bar{y}\boldsymbol{\Lambda}\mathbf{v} \otimes \boldsymbol{\mu} + \kappa_0 \bar{y}\mathbf{v} \otimes \mathbf{A}\mathbf{T}^{-1}\boldsymbol{\mu} = \mathbf{0}. \quad (35)$$

The equation for the concentration observable $U_i = \mathbf{e}_K^T \mathbf{u}_i$ in $\mathcal{V}_i$ [cf. (10)] is, by (26) and (24),

$$U_{it} = \gamma_0\left(\sum_{j\in\mathcal{J}(i)} D_{ij}\mathbf{e}_K^T\mathbf{T}\mathbf{u}_j + D_{ii}\mathbf{e}_K^T\mathbf{T}\mathbf{u}_i\right). \quad (36)$$

An explicit equation for U_i is obtained if we knew the diffusion coefficient

$$\hat{\gamma}_j(t) = \gamma_0 \mathbf{e}_K^T \mathbf{T}\mathbf{u}_j / U_j \quad (37)$$

in $\mathcal{V}_j$. Then, by (25), (36) is rewritten

$$U_{it} = \sum_{j\in\mathcal{J}(i)} \hat{\gamma}_j(t)\frac{S_{ij}}{|\mathcal{V}_i|}U_j + \hat{\gamma}_i(t)\frac{S_{ii}}{|\mathcal{V}_i|}U_i. \quad (38)$$

The stiffness matrix with a variable diffusion in space and time in (12) is

$$\begin{aligned}\tilde{S}_{ij}(t) &= -\sum_{E_\alpha\in\mathcal{T}_{ij}} \int_{E_\alpha} \nabla\varphi_i^T|_{E_\alpha}\tilde{\gamma}(\mathbf{x},t)\nabla\varphi_j|_{E_\alpha}\, d\mathbf{x} \\ &= -\sum_{E_\alpha\in\mathcal{T}_{ij}} \nabla\varphi_i^T|_{E_\alpha}\nabla\varphi_j|_{E_\alpha}\tilde{\gamma}_\alpha(t)|E_\alpha| = \tilde{\gamma}_{ij}(t)S_{ij}, \quad (39)\end{aligned}$$

where $\tilde{\gamma}_\alpha$ is the spatial average of $\gamma(\mathbf{x}, t)$ in element E_α and the last equality defines $\tilde{\gamma}_{ij}$ as in (18). Then, using $\tilde{S}_{ij}$ in (39), the discretization of (12) is

$$\begin{aligned}U_{it} &= \sum_{j\in\mathcal{I}(i)} \frac{\tilde{S}_{ij}}{|\mathcal{V}_i|}U_j + \frac{\tilde{S}_{ii}}{|\mathcal{V}_i|}U_i \\ &= \sum_{j\in\mathcal{I}(i)} \tilde{\gamma}_{ij}(t)\frac{S_{ij}}{|\mathcal{V}_i|}U_j + \tilde{\gamma}_{ii}(t)\frac{S_{ii}}{|\mathcal{V}_i|}U_i. \quad (40)\end{aligned}$$

Thus, (38) is a discretization of (12) with a time varying $\hat{\gamma}_j$. The diffusion coefficient $\tilde{\gamma}_{ij}$ along the edges in the direct discretization of (12) in (40) is approximated by $\hat{\gamma}_j$ at the nodes in (38).

The partitioning of the internal state space Ξ into intervals $\mathcal{I}_k = [\xi_{k-1}, \xi_k]$ is generalized somewhat by allowing intervals of different length $\Delta\xi_k = \xi_k - \xi_{k-1}$ where the ξ_k's no longer are equidistant. Let $\boldsymbol{\delta}^T = (\Delta\xi_1, \ldots, \Delta\xi_K)$ and let $\boldsymbol{\Delta}$ be a diagonal matrix with $\Delta\xi_k$ on the diagonal. Then, the discrete relations corresponding to (9), (13), and (14) are

$$\boldsymbol{\delta}^T\mathbf{A} = \mathbf{0},\ \mathbf{A} = (\boldsymbol{\mu}\boldsymbol{\delta}^T - \mathbf{I}_K)\mathbf{T},\ \boldsymbol{\delta}^T\boldsymbol{\mu} = 1 \quad (41)$$

[cf. (24)]. The null vector $\mathbf{u}_{i\infty}$ of $\mathbf{A}$ satisfies the same equation as in (24). The relation between the concentration in voxel i and internal state k and the copy number in the same voxel and state is $u_{ik} = |\mathcal{V}_i|^{-1}\Delta\xi_k^{-1}\bar{y}_{ik}$. Multiply the equation for $\mathbf{u}_i$ [Eq. (27)] by $|\mathcal{V}_i|$ and $\boldsymbol{\Delta}$ to obtain an equation for $\bar{\mathbf{y}}_i$ as in (28). Then, the new $\mathbf{T}_\Delta$ and the new $\mathbf{A}_\Delta$ in (27) will be

$$\begin{aligned}\mathbf{T}_\Delta &= \boldsymbol{\Delta}\mathbf{T}\boldsymbol{\Delta}^{-1} = \mathbf{T}, \\ \mathbf{A}_\Delta &= \boldsymbol{\Delta}\mathbf{A}\boldsymbol{\Delta}^{-1} = \boldsymbol{\Delta}\boldsymbol{\mu}\boldsymbol{\delta}^T\mathbf{T}\boldsymbol{\Delta}^{-1} - \mathbf{T} \\ &= \left(\boldsymbol{\Delta}\boldsymbol{\mu}\mathbf{e}_K^T - \mathbf{I}_K\right)\mathbf{T} \quad (42)\end{aligned}$$

since $\mathbf{T}$ is diagonal. This $\mathbf{A}_\Delta$ replaces $\mathbf{A}$ in Eqs. (28), (30), (34), and (35) for $\bar{\mathbf{y}}_i$. By allowing variable $\Delta\xi_k$, better resolution of parts of Ξ can be achieved, but in order to simplify the notation, we assume henceforth that the interval length is constant $\Delta\xi_k = \Delta\xi$.

3. *Several species and reactions*

Assume that the diffusion coefficient γ_0 and that the transition matrix $\mathbf{A}$ are the same for all species in the system. The components of the copy number vector $\bar{\mathbf{y}}$ in (28) are $\bar{y}_{ik\ell}$ where $\ell = 1, 2, \ldots, L$, denotes the molecular species. The reactions are assumed to be the same in every voxel independent of space, depending only on the copy number in the voxel as in (6). They are also assumed to be the same in each internal state except for a scaling with $\mathbf{G}$. In model I for the reactions in [47], $\mathbf{G} = \mathbf{T}$, and in model II, $\mathbf{G} = \mathbf{I}$. Then, the reaction-diffusion equation is derived by adding a reaction term $\mathbf{e}_J \otimes \mathbf{g} \otimes \mathbf{f}$ with $\mathbf{g} = \mathbf{G}\mathbf{e}_K$ to (26), thus extending the solution $\bar{\mathbf{y}}$ in (28) by the number of molecules of the different species. In the reaction term, $\mathbf{f}$ in the $e_i g_k \mathbf{f}$ element of $\mathbf{e}_J \otimes \mathbf{g} \otimes \mathbf{f}$ in voxel $\mathcal{V}_i$ and internal state k depends on $\bar{\mathbf{y}}_{ik} \in \mathbb{R}^L$, the state vector of copy numbers of the L different species in $\mathcal{V}_i$ in internal state k. Including reactions, Eq. (35) then becomes

$$\begin{aligned}\bar{\mathbf{y}}_t &= \gamma_0(\boldsymbol{\Lambda} \otimes \mathbf{T} \otimes \mathbf{I}_L)\bar{\mathbf{y}} \\ &\quad + \kappa_0(\mathbf{I}_J \otimes \mathbf{A} \otimes \mathbf{I}_L)\bar{\mathbf{y}} + \mathbf{e}_J \otimes \mathbf{g} \otimes \mathbf{f}. \quad (43)\end{aligned}$$

Unless $\mathbf{f}$ is affine in $\bar{\mathbf{y}}$, the solution of this macroscopic reaction-diffusion equation only approximates the mean values of the number of molecules in the mesoscopic model (see, e.g., [55]). If $\mathbf{T} = \mathbf{I}_K$ in (43), then the diffusion is the same for the molecules in all internal states but the reaction rates in $\mathbf{f}$ may still be dependent on the internal states.

III. CONNECTING THE MULTISCALE AND THE INTERNAL STATES MODELS

A constructive procedure to incorporate the coarse-grained diffusion coefficients into the internal state framework is proposed in this section. Briefly, the computed statistical distribution of the effective diffusion rates due to different possible crowder distributions is used to determine the parameters in the internal state model. The crowding model induces errors caused by the discretization, the statistics, and the coarse graining. These inaccuracies are analyzed and alternative ways to obtain the necessary data are discussed.

A. Coarse graining the diffusion coefficient

If the obstacles are stationary and their shapes and positions are known, then the effect of the crowding can be computed directly as in Sec. II A and there is no need for internal states.

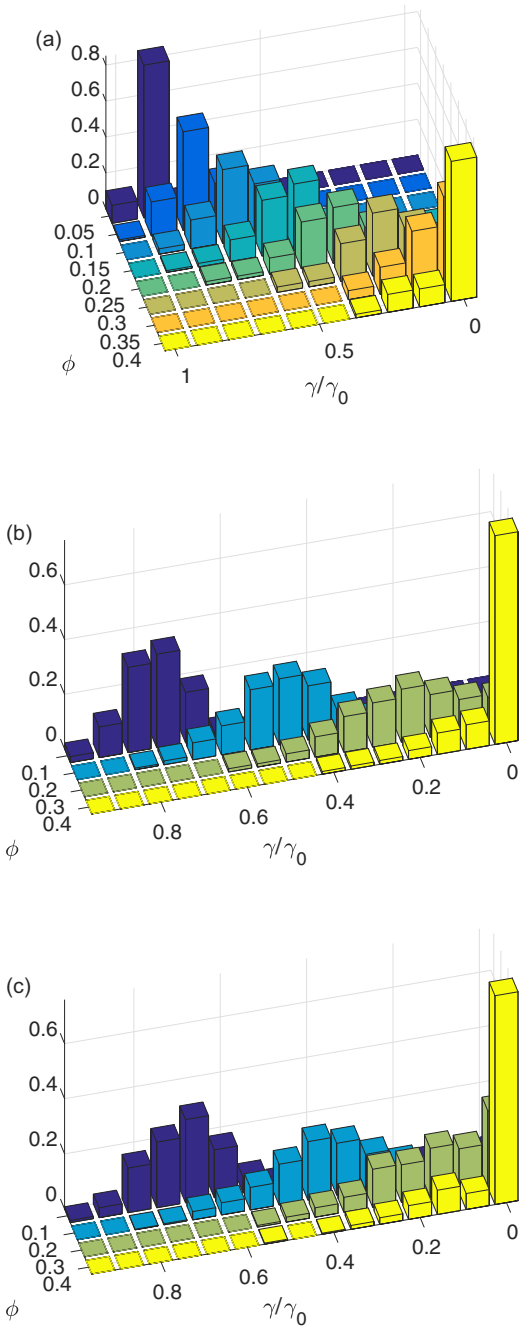

FIG. 3. Histogram counts of γ/γ_0 for different fractions of occupied volume ϕ. (a) Detailed resolution in ϕ with $K = 10$ bins for $Q = 100$ different circular crowder distributions in 2D, where $R/\rho = 0.1$ and $r/\rho = 0.1$. (b), (c) Less resolution in ϕ and finer resolution in the internal states with $K = 15$ bins for $Q = 500$ different crowder distributions with circular obstacles (b) and a mix of circular and rectangular obstacles (c).

If the obstacles are mobile, it would be too expensive computationally to determine a $\gamma(t)$ in every time step of a discretized equation (40) and also all details of how the obstacles are moving are likely not known. Instead, γ is sampled from a stationary distribution. This distribution is computed with a circle or sphere of radius ρ circumscribing a voxel of a typical size in the mesh as in Fig. 2. The tracer is a circle with radius r and the obstacles are either circles with radius R or rectangles with the same area. The obstacles are randomly distributed inside ω_* for a given percentage of occupied volume ϕ. Then, we compute γ by evaluating (5) at the center $\mathbf{x}_0$ and collect statistics. These distributions effectively approximate the probability density function (PDF) $p_\gamma(\gamma, \phi)$ (see Fig. 3), and the joint distribution for γ and ϕ can be determined if the PDF $p_\phi(\phi)$ of ϕ is known. In Fig. 3(c), the tracer is circular and half of the crowders are circular and the other half are rectangles with the same area and a side ratio of about $1:5$. When $0.1 < \phi < 0.25$ the γ distributions are close to normal. When $\phi > 0.3$ the molecule will not reach $\partial\omega_*$ for many obstacle configurations implying that $E(\mathbf{x}) \to \infty$ and $\gamma/\gamma_0 \to 0$ in (5). Since elongated obstacles impede the diffusion of tracer molecules more effectively [38], the distributions with mixed crowder distributions in Fig. 3(c) are shifted towards 0 compared to those with only circular crowders in Fig. 3(b) leading to a slower effective diffusion γ.

The effects of a deterministic $\phi(\mathbf{x})$ variable in space are studied in [56]. Sampling a new γ for the moving molecule after Δt accounts in [56] for the movement of the crowder molecules during that time step. This γ sampling corresponds to the molecules switching their internal states, and we will couple the statistics in Fig. 3 to $\mathbf{A}$ and $\mathbf{T}$ in (30) in the next section.

B. Diffusion coefficients in internal states

A molecule in different internal states k in Sec. II B has different diffusion coefficients γ_k and switches its state according to $\kappa_0\mathbf{A}$. We sample these γ_k from the stationary distributions in Sec. III A for a given ϕ and the frequency of the state k being f_k. The elements of $\mathbf{A}$ are computed using γ_k and f_k.

Let τ be the overall time scale for the speed of switching of the internal states and let $\kappa_0 = 1/\tau$. A large τ with $\kappa_0 \ll \gamma_0$ implies that the timescale of switching the internal states is slower than the scale of diffusion. A physical interpretation is that the crowding obstacles move slowly and the tracer hence diffuses with the same γ_k for a long time. If instead τ is small, then the motion of the obstacles is fast compared to the tracer molecules.

The quotient between the diffusion coefficient with crowding γ_k in internal state k obtained by coarse graining and the coefficient γ_0 in free space is denoted by $\theta_k = \gamma_k/\gamma_0 \in [0, 1]$. The diffusion in the kth internal state in (26), (27), and (28) is

$$\gamma_k = \gamma_0\theta_k = \gamma_0 T_{kk}. \tag{44}$$

Hence, $T_{kk} = \theta_k$. Let the ordering of the internal states be such that $\gamma_k \leqslant \gamma_{k+1}$.

The stationary distribution in the internal states is $\mu_k/T_{kk} = \mu_k/\theta_k$, $k = 1, \ldots, K$, in (15) and (24). We now set this stationary distribution proportional to the frequency f_k of the state k computed by the homogenization in Sec. III A:

$$\frac{\mu_k}{\theta_k} \propto f_k,$$

and after normalizing with $\sum_{j=1}^K \mu_j = 1$ we obtain

$$\mu_k = \frac{f_k\theta_k}{\sum_{j=1}^K f_j\theta_j}. \tag{45}$$

The transfer matrix in (13) and (24) is defined by

$$A_{ij} = \mu_i \theta_j, \ i \neq j, \quad A_{ii} = (\mu_i - 1)\theta_i, \tag{46}$$

as in [47]. The stationary probability $p_k = p(\gamma_k|\phi)$ to be in internal state k is proportional to f_k and μ_k/θ_k. With a scaling such that $\sum_{j=1}^K p_j = 1$, we have

$$p_k = \frac{f_k}{\sum_{j=1}^K f_j} = \frac{\mu_k/\theta_k}{\sum_{j=1}^K \mu_j/\theta_j}. \tag{47}$$

Using (44) and (47), the expected diffusion rate for a molecule in the stationary state is

$$\bar{\gamma} = \sum_{j=1}^K \gamma_j p_j = \gamma_0 \frac{\sum_{j=1}^K f_j \theta_j}{\sum_{j=1}^K f_j} \leqslant \gamma_0, \tag{48}$$

and the variance scaled by the square of the mean is

$$\frac{\mathrm{var}[\gamma]}{\bar{\gamma}^2} = \bar{\gamma}^{-2} \sum_{j=1}^K (\gamma_j - \bar{\gamma})^2 p_j = \sum_{j=1}^K \frac{\mu_j}{\theta_j} \sum_{j=1}^K \mu_j \theta_j - 1. \tag{49}$$

The mean diffusion coefficient $\bar{\gamma}$ in (48) is reduced compared to diffusion in free space γ_0 if at least one $\theta_k < 1$. Both $\mathbf{A}$ in (46) and $\bar{\gamma}$ in (48) are determined uniquely by γ_k and the corresponding f_k.

The statistics in Fig. 3 can be used to introduce more internal states to represent also different crowding densities ϕ_j. Both γ_i and ϕ_j are then sampled from the joint distribution by changing the internal states.

C. Uncertainty quantification

The dynamics of the internal state model in $\mathbf{A}$ and the stationary solution μ_k/θ_k are determined by θ_k and μ_k. The data f_k, p_k, and γ_k may be contaminated by errors Δf, Δp, and $\Delta\gamma$ which propagate to θ_k and μ_k and the stationary solution. Three types of errors are considered here: a statistical error, an approximation error, and a model error. The space $\Xi = [0, 1]$ is partitioned into K bins of size $\Delta\xi = 1/K$ with γ_k/γ_0 as the midpoint in the kth interval in Sec. III A and Fig. 3.

In the figures, Q random distributions of obstacles are first generated and then the viscosity γ/γ_0 is computed by (5). The random variable F_k counts the number of samples with γ/γ_0 in the kth bin. The probability to be in bin k is π_k with $\sum_k \pi_k = 1$. The distribution of F_k is multinomial with mean $Q\pi_k$ and variance $Q\pi_k(1 - \pi_k)$. We take the standard deviation $\sqrt{Q\pi_k(1 - \pi_k)}$ as an estimate of the statistical error Δf_k in f_k. Since $\sum_k f_k = Q$ it follows from (47) that p_k estimates π_k and as the error in p_k we take the sample standard deviation $\Delta p_k = \sqrt{p_k(1 - p_k)/Q}$. This error is reduced by increasing the number of samples Q. The statistical error at $\phi = 0.2$ and $\theta_5 = 0.45$ in Fig. 3 is estimated to be $\Delta p_5 \approx \sqrt{0.4 \times 0.6/100} \approx 0.05$.

Recalling that θ equals γ scaled by γ_0 in (44), a smooth PDF $\pi(\theta)$ is approximated by a step function $\sum_k p_k \psi_k(\theta)$ in Fig. 3 where ψ_k is defined in the beginning of Sec. II B 2. The difference between π and the sum has a leading term in the interval $\mathcal{I}_k$ which is

$$\pi(\theta) - p_k = \pi'(\theta_k)(\theta - \theta_k).$$

Thus, the error in the PDF in $\mathcal{I}_k$ is bounded by $\Delta p_k \leqslant \max_{\theta\in\mathcal{I}_k} |\pi_k'||\theta - \theta_k| \leqslant |\pi_k'|/2K$. This error is reduced by increasing K. A bound on the approximation error at $\phi = 0.2$ and $\theta_6 = 0.55$ in Fig. 3 is $\Delta p_6 \leqslant 1.5/2 \times 10 = 0.075$ since $\pi_6' \approx 1.5$.

In [38, Fig. 4(e)], the θ values determined by (5) are compared to θ_{BD} obtained by BD simulations with the same obstacle distribution using Smoldyn [39]. The BD model is considered to be more accurate and the comparison is a test that the procedure behind (5) is accurate. This is expected since the solution to (2) is the analytical mean first exit time for a particle moving with Brownian diffusion in Ω. Possible causes of bias in (5) are the numerical solution of (2), the release of the molecule in the center of the circle, and the restriction to distributions where there is no obstacle in the center. The sources of error in θ_{BD} are the number of BD trajectories and the finite length of the time steps in the simulation. The θ from (5) is in the middle of the interval $[\theta_{\mathrm{BD}} - \Delta\theta, \theta_{\mathrm{BD}} + \Delta\theta]$ where $\Delta\theta \approx 0.05$ for $\phi = 0.1$ and $\Delta\theta \approx 0.1$ for $\phi = 0.3$ in [38]. This deviation is likely to decrease with more BD simulation samples.

The errors in p_k and θ_k will cause an error $\Delta\mu_k$ in μ_k and the stationary solution $u_{i\infty k} = \mu_k/\theta_k$. It follows from (45), (47), and (48) that $\mu_k = p_k\gamma_k/\bar{\gamma}$ and the dominant term in the perturbation due to the statistical or approximation error

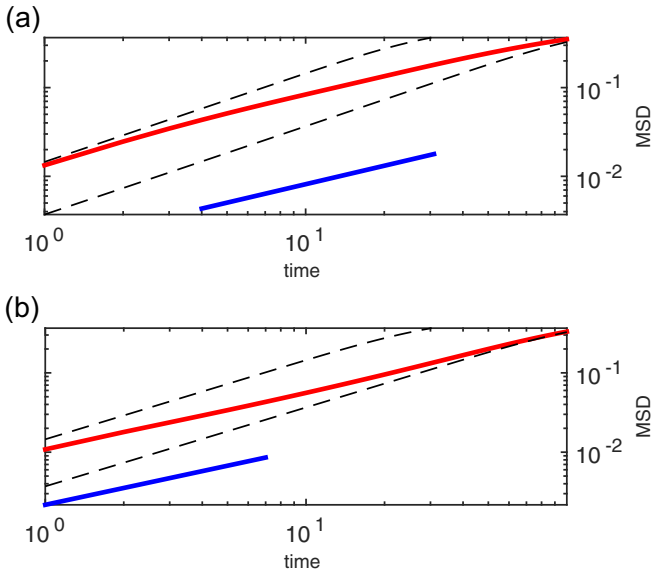

FIG. 4. Simulation of coarse-grained subdiffusion in 2D. (a) The mean-square displacement as a function of time (top solid red). The dashed curves are obtained with the initial and the steady state diffusion, γ_0 and $\bar{\gamma}$, and the slope of the comparison curve t^α is $\alpha = 0.7$ (bottom solid blue). (b) As above, but with a four times faster diffusion of obstacles and hence faster scaling of time for the switching between internal states, $\kappa_0 \to 4\kappa_0$, resulting in a faster approach to the steady state diffusion (but still such that $\alpha = 0.7$ for the comparison slope). These plots are computed with data for $\phi = 0.35$ in Fig. 3(a).

Δp_k is

$$\Delta\mu_k = \Delta p_k \frac{\gamma_k}{\bar{\gamma}}. \tag{50}$$

Thus, the stationary solution is perturbed by $\Delta\mu_k/\theta_k = \Delta p_k\gamma_0/\bar{\gamma}$. Since $u_{i\infty k} = p_k\gamma_0/\bar{\gamma}$, a perturbation $\Delta\theta_j$ in θ_j will introduce a relative error $\Delta u_{i\infty k}/u_{i\infty k}$ in the stationary solution which is

$$\begin{aligned}\frac{\Delta u_{i\infty k}}{u_{i\infty k}} &= \left(\frac{p_k\gamma_0}{\bar{\gamma}+p_j\Delta\gamma_j} - \frac{p_k\gamma_0}{\bar{\gamma}}\right)\Big/ u_{i\infty k} \\ &= -p_j\frac{\Delta\gamma_j}{\bar{\gamma}} = -p_j\frac{\gamma_0}{\bar{\gamma}}\Delta\theta_j. \end{aligned}\tag{51}$$

In Fig. 3, $\gamma_0/\bar{\gamma} \approx 1.3$ for $\phi = 0.1$ and with $|\Delta\theta_j| \leqslant 0.05$ the relative error is $|\Delta u_{i\infty k}/u_{i\infty k}| \leqslant 0.065 p_j$ independent of k. To conclude, all pieces of the numerical model are subject to uncertainties which can be controlled by employing a more accurate but also more costly numerical setup.

D. Alternatives

The coefficients μ_k and θ_k and the probability mass function p_k, $k = 1, \ldots, K$, are determined from collected coarse-grained data for the diffusion in crowded environments in Sec. III A. It is sufficient to know f_k or p_k for γ_k or γ_k/γ_0 where $\gamma_0 = \max_k \gamma_k$ to derive μ_k and θ_k in (44) and (47). These parameters can be obtained from other sources than in Secs. II A and III A.

In [46] and [47, Sec. 4.1], α in (1) is given. Then, μ_k, θ_k, and p_k are computed for this α in an approximation of the waiting time for the next diffusive jump to take place. If a distribution for α is known as in [57,58] from observations of trajectories, then since $p(\gamma) = \int_0^1 p(\gamma|\alpha)p(\alpha)\,d\alpha$ a quadrature rule for p_k is $p_k = \sum_{l=1}^{L} p(\gamma_k|\alpha_l)p(\alpha_l)/L$ with α_l chosen equidistantly in [0, 1].

The concept of diffusing diffusivity is introduced in [59]. The purpose is to be able to reproduce the observed behavior that the MSD is linear in t, yet the distribution of the displacement is non-Gaussian for a short time. Then, there is a crossover in time and after that the distribution is Gaussian. The diffusion coefficient varies randomly in time with a stationary distribution of γ, $p_k \sim \exp(-\gamma_k/\gamma_*)$ where γ_* is a scaling factor of the diffusion. Such a distribution is close to the ones for $\phi \geqslant 0.35$ in Fig. 3. This model is analyzed in [59,60].

In general, p_k can be determined by Bayesian methods using data on the motion of molecules. Suppose that trajectories of molecules are available, either from experiments or simulations with BD, then a Markov chain Monte Carlo (MCMC) algorithm [61] computes the PDF of the distribution of γ.

IV. ANALYTICAL DISTRIBUTIONS

Consider an open chemical system with the monomolecular reactions degradation, conversion, and production from a source and include diffusion between voxels i and j and a switch of internal states between k and l. Then, the transformations of the species are

$$\begin{aligned} &A_{ik} \rightleftharpoons A_{jk},\ A_{ik} \rightleftharpoons A_{il},\ A_{ik} \longrightarrow B_{ik}, \\ &A_{ik} \longrightarrow \emptyset,\ \emptyset \longrightarrow A_{ik}. \end{aligned}\tag{52}$$

In order from left to right, the reactions in (52) are as follows: change of voxel by diffusion, change of internal state in a voxel, conversion from A to B in the same voxel and internal state, degradation of A, and production of A. When the reaction propensities are independent of, or linear in, the copy numbers, the expression for the probability distribution of molecules solving the reaction-diffusion master equation is known explicitly at the stochastic, mesoscopic level of modeling (see [55,62]).

The analytical solutions of the PDFs of the chemical networks in (52) are in this section used to derive the macroscopic diffusion coefficient in (37) and the statistical properties of the random molecular numbers of the species in the steady state. It is shown that the copy numbers of the molecules in the voxels are multinomially distributed where the parameters satisfy a system of ordinary differential equations of the same type as in Sec. II B 2. This system has a solution in agreement with the solutions in Sec. III B and can be solved explicitly in the steady state.

A random vector $\mathbf{Y}$ with entries $Y_{ik\ell}$ is the state vector for the copy number of species ℓ in internal state k in voxel i. The mean value of $\mathbf{Y}$ is denoted by $\bar{\mathbf{y}}$ in Sec. II B 2. We determine the probability distribution of $\mathbf{Y}$ analytically for the transformations in (52).

If the chemical system has the monomolecular reactions conversion and degradation as in (52) except for the production of A, then the system is closed and $\mathbf{f}$ in (43) in voxel i in internal state k is

$$\mathbf{f}(\bar{\mathbf{y}}_{ik}) = \mathbf{R}\bar{\mathbf{y}}_{ik}, \tag{53}$$

where $\mathbf{R}$ is constant and $\mathbf{R} \in \mathbb{R}^{L\times L}$. For such an $\mathbf{f}$ we have the stationary solution $\bar{\mathbf{y}}_{ik\infty}$ satisfying

$$\mathbf{R}\bar{\mathbf{y}}_{ik\infty} = \mathbf{0}. \tag{54}$$

Initially, there are N molecules in the system. If $\emptyset$ is regarded as a special species, then the number of molecules N is constant. No molecules are created and no molecules disappear. If there is degradation, the system may end up with all molecules in $\emptyset$.

The PDF of the multinomial distribution $\mathcal{M}(N, \mathbf{p})$ for $\mathbf{y}$ with $M = JKL$ states is

$$p_{\mathcal{M}}(\mathbf{y}, \mathbf{p}) = \frac{N!}{y_1!\cdot y_2!\ldots y_M!} p_1^{y_1} p_2^{y_2}\ldots p_M^{y_M},\ \sum_{m=1}^{M} y_m = N. \tag{55}$$

Here, m is the global index $m = 1 + (j-1) + (k-1)J + (l-1)JK$ for the state jkl to simplify the notation. The probability for a molecule to be in state m at t is $p_m(t)$ and hence $\sum_{m=1}^{M} p_m = 1$, $p_m \geqslant 0$. Assume that the initial distribution of $\mathbf{Y}$ at $t = 0$ in the chemical system is $\mathcal{M}(N, \mathbf{p}_0)$. Then, it is proved in [62] that the joint distribution of $\mathbf{Y}$ for all molecules for $t > 0$ is multinomial $\mathcal{M}(N, \mathbf{p}(t))$ where $\mathbf{p}(t)$ solves

$$\begin{aligned} \mathbf{p}_t = \mathbf{B}\mathbf{p}, \quad \mathbf{B} &= \gamma_0\mathbf{\Lambda}\otimes\mathbf{T}\otimes\mathbf{I}_L \\ &+ \kappa_0\mathbf{I}_J\otimes\mathbf{A}\otimes\mathbf{I}_L + \mathbf{I}_J\otimes\mathbf{G}\otimes\mathbf{R}, \end{aligned}\tag{56}$$

with initial data $\mathbf{p}(0) = \mathbf{p}_0$. The system matrix $\mathbf{B}$ is identical to the one in (43) where

$$\mathbf{e}_J \otimes \mathbf{g} \otimes \mathbf{f} = \mathbf{I}_J \otimes \mathbf{G} \otimes \mathbf{R}\mathbf{p}$$

for our monomolecular reactions.

Let $\mathcal{W}_w$, $w = 1, \ldots, W$, be subsets of $\mathcal{I}_M = \{1, 2, \ldots, M\}$ such that $\bigcup_{w=1}^{W} \mathcal{W}_w = \mathcal{I}_M$ and introduce

$$Z_w = \sum_{m \in \mathcal{W}_w} Y_m, \quad q_w = \sum_{m \in \mathcal{W}_w} p_m, \quad \mathbf{z} \in \mathbb{R}^W. \tag{57}$$

Then, by the properties of the multinomial distribution, the PDF of $\mathbf{Z}$ is

$$P(t, \mathbf{z}) = p_{\mathcal{M}}(\mathbf{z}, \mathbf{q}(t)). \tag{58}$$

In particular, if $\mathbf{z} \in \mathbb{N}^2$, i.e., $W = 2$ and z_w is integer and non-negative, then the distribution is binomial.

The stationary distribution when $t \to \infty$ is

$$\lim_{t \to \infty} P(t, \mathbf{y}) = p_{\mathcal{M}}(\mathbf{y}, \mathbf{p}_\infty), \tag{59}$$

where $\mathbf{p}_\infty$ is the solution of

$$\mathbf{B}\mathbf{p}_\infty = 0. \tag{60}$$

The vectors $\mathbf{v}$ with $v_i = |\mathcal{V}_i|$ and $\mathbf{T}^{-1}\boldsymbol{\mu}$ satisfy $\boldsymbol{\Lambda}\mathbf{v} = \mathbf{0}$ and $\mathbf{A}\mathbf{T}^{-1}\boldsymbol{\mu} = \mathbf{0}$ as in (35). Let $\mathbf{p}_{\Lambda\infty}$, $\mathbf{p}_{A\infty}$, and $\mathbf{p}_{R\infty}$ satisfy

$$\mathbf{p}_{\Lambda\infty} = \eta_\Lambda \mathbf{v}, \ \mathbf{p}_{A\infty} = \eta_A \mathbf{T}^{-1}\boldsymbol{\mu}, \ \mathbf{R}\mathbf{p}_{R\infty} = \mathbf{0}, \tag{61}$$

with $\mathbf{p}_{R\infty}$ and scalings η_Λ and η_R chosen to fulfill $\|\mathbf{p}_{\Lambda\infty}\|_1 = \|\mathbf{p}_{A\infty}\|_1 = \|\mathbf{p}_{R\infty}\|_1 = 1$. The stationary distributions $\mathbf{p}_{\Lambda\infty}$, $\mathbf{p}_{A\infty}$, and $\mathbf{p}_{R\infty}$ are all independent of γ_0 and κ_0. If the reaction matrix $\mathbf{R}$ is irreducible such that the chemical network cannot be decomposed into two or more independent networks, then there is a $\mathbf{p}_{R\infty}$ with non-negative components $p_{R\infty,i}$ in (61) [55,62]. It follows from (60), (56), and (61) that

$$\mathbf{p}_\infty = \mathbf{p}_{\Lambda\infty} \otimes \mathbf{p}_{A\infty} \otimes \mathbf{p}_{R\infty}, \ \|\mathbf{p}_\infty\|_1 = 1. \tag{62}$$

With the conversion reaction in (52), $\mathbf{R}$ is such that $\mathbf{e}_L^T\mathbf{R} = \mathbf{0}$. It follows from (32) and (56) that

$$(\mathbf{e}_J \otimes \mathbf{e}_K \otimes \mathbf{e}_L)^T \mathbf{B} = \mathbf{0}. \tag{63}$$

Using (56), we find that

$$\left(\mathbf{e}_J \otimes \mathbf{e}_K \otimes \mathbf{e}_L^T\mathbf{p}\right)_t = (\mathbf{e}_J \otimes \mathbf{e}_K \otimes \mathbf{e}_L)^T \mathbf{p}_t = \mathbf{0}, \tag{64}$$

and the probability is preserved

$$\|\mathbf{p}(t)\|_1 = \|\mathbf{p}(0)\|_1 = \|\mathbf{p}_\infty\|_1 = 1, \tag{65}$$

with a properly chosen initial solution $\mathbf{p}_0 = \mathbf{p}(0)$.

When the timescale of the diffusion is fast with a large $\tau = \kappa_0^{-1} \gg \gamma_0^{-1}$, then by (46) $\kappa_0\mathbf{A}$ is negligible in (56) since $\mathbf{A}$ is of $O(1)$. Spatial gradients disappear rapidly and the system becomes well stirred. On the contrary, if τ is small, then $\kappa_0\mathbf{A}$ dominates and there is a fast equilibration in the internal states such that the solution is (after reordering the unknowns $p_{ik\ell}$) $\mathbf{p}(t) \approx \mathbf{p}'(t) \otimes \mathbf{p}_{A\infty}$ and $\mathbf{I}_J \otimes \mathbf{I}_L \otimes \mathbf{A}\mathbf{p} \approx (\mathbf{I}_J \otimes \mathbf{I}_L)\mathbf{p}' \otimes \mathbf{A}\mathbf{p}_{A\infty} = \mathbf{0}$ in the second term in $\mathbf{B}$ in (56).

The expected value $u_{ik\ell}$ of the concentration of species ℓ in voxel i and internal state k is given by

$$u_{ik\ell}(t) = E\left[\frac{Y_{ik\ell}}{|\mathcal{V}_i|}\right] = \frac{N}{|\mathcal{V}_i|} p_{ik\ell}(t) = \frac{\bar{y}_{ikl}}{|\mathcal{V}_i|}. \tag{66}$$

Since the mean values of the copy numbers $\bar{\mathbf{y}}(t)$ satisfy (56), $\mathbf{u}$ in (66) satisfies an equation like (26) with an additional reaction term.

The diffusion coefficient in the equation for the observable $U_{i\ell}$ in (38) in voxel i and species ℓ with $\mathbf{e}_K^T\mathbf{p}_{i\ell}(t) > 0$ is by (37), (66), and (44):

$$\hat{\gamma}_{i\ell}(t) = \gamma_0 \frac{\mathbf{e}_K^T\mathbf{T}\mathbf{p}_{i\ell}(t)}{\mathbf{e}_K^T\mathbf{p}_{i\ell}(t)} = \gamma_0 \frac{\sum_{k=1}^K \theta_k p_{ik\ell}(t)}{\sum_{k=1}^K p_{ik\ell}(t)} \leqslant \gamma_0 \tag{67}$$

since $0 \leqslant \theta_j \leqslant 1$ [cf. (48) for the stationary case]. The time dependent diffusion coefficient $\hat{\gamma}_{i\ell}(t)$ depends on $\mathbf{p}_0$ and the dynamics of $\mathbf{B}$ in (56). It is bounded from above by the nominal coefficient γ_0 and as $t \to \infty$, $\hat{\gamma}_{i\ell}(t)$ approaches $\bar{\gamma}$ in (48).

Suppose that the error in θ_k satisfies $|\Delta\theta_k| \leqslant \Delta\theta$. Such a bound can be determined from the formulas in Sec. III C. Then, a bound on the error in $\hat{\gamma}_{i\ell}$ in (67) is

$$|\Delta\hat{\gamma}_{i\ell}(t)| = \gamma_0 \left| \frac{\sum_{k=1}^K \Delta\theta_k p_{ik\ell}(t)}{\sum_{k=1}^K p_{ik\ell}(t)} \right| \leqslant \gamma_0 \Delta\theta. \tag{68}$$

A simpler alternative to $\hat{\gamma}$ in (67) is to derive the random diffusion field in (38) as follows. First, discretize the time derivative in (38) at t^n, $n = 0, 1, \ldots$, and sample $\hat{\gamma}_j^n$ with the stationary distribution in (47). Then, we have a numerical approximation of the parabolic PDE (12) discretized by finite elements in (38) with a random, space and time dependent diffusion coefficient field $\tilde{\gamma}$ with mean and variance (48) and (49).

The sum of the molecules over the internal states in each voxel and for each species is denoted by

$$Z_{i\ell} = \sum_{k=1}^K Y_{ik\ell}. \tag{69}$$

Since $\mathbf{Y}$ is multinomially distributed with parameters $\mathbf{p}$, $\mathbf{Z}$ is also multinomially distributed $\mathcal{M}(N, \mathbf{q})$ according to (57) and (58) where $\mathbf{q}$ has the components

$$q_{i\ell}(t) = \sum_{k=1}^K p_{ik\ell}(t). \tag{70}$$

At the stationary distribution, $\mathbf{q}$ is

$$q_{i\ell\infty} = \sum_{k=1}^K p_{\Lambda\infty,i} p_{A\infty,k} p_{R\infty,\ell} = p_{\Lambda\infty,i} p_{R\infty,\ell}. \tag{71}$$

The observable $U_{i\ell}$ is the expected value of the concentration of species ℓ in $\mathcal{V}_i$:

$$U_{i\ell}(t) = \mathrm{E}\left[\frac{Z_{i\ell}}{|\mathcal{V}_i|}\right] = \frac{N}{|\mathcal{V}_i|} q_{i\ell}(t). \tag{72}$$

Using (71), we find that the steady state solution $U_{\infty,i\ell}$ is independent of i and thus constant in space. The variance of the concentration is

$$\mathrm{var}\left[\frac{Z_{i\ell}}{|\mathcal{V}_i|}\right] = \frac{N}{|\mathcal{V}_i|^2} q_{i\ell}(t)[1 - q_{i\ell}(t)]. \tag{73}$$

The number of voxels J is often large making $q_{i\ell}(t) \propto 1/JL$ and small and the variance is approximately $Nq_{i\ell}(t)/|\mathcal{V}_i|^2 = U_{i\ell}/|\mathcal{V}_i|$. The covariance between species ℓ in voxel i and species m in voxel j is

$$\mathrm{cov}\left[\frac{Z_{i\ell}}{|\mathcal{V}_i|}, \frac{Z_{jm}}{|\mathcal{V}_j|}\right] = -\frac{N}{|\mathcal{V}_i||\mathcal{V}_j|} q_{i\ell}(t) q_{jm}(t). \tag{74}$$

The covariation between the voxels is negative and since $q_{i\ell}$ is usually small, it is very small. The mean and the variance of the copy numbers $Z_{i\ell}$ are

$$E[Z_{i\ell}] = Nq_{i\ell}(t), \quad \mathrm{var}[Z_{i\ell}] = Nq_{i\ell}(t)[1 - q_{i\ell}(t)]. \tag{75}$$

The Fano factor $\mathrm{var}[Z_{i\ell}]/E[Z_{i\ell}]$ is $1 - q_{i\ell}(t)$ and close to 1, which is the factor of a Poisson process.

A similar analysis is possible for a chemical system when all monomolecular reactions in (52) are included. If the copy numbers $\mathbf{Y}$ in the states of the system are Poisson distributed initially, then they will remain Poisson distributed with rate parameters satisfying an equation like (56) and (43) (see [62]).

V. NUMERICAL EXAMPLES

We now proceed to illustrate the behavior of the suggested coarse-grained model of subdiffusion in stochastic simulation of trajectories of the chemical network. After first briefly summarizing the simulation algorithm in Sec. V A, we look at the mean-square displacement of subdiffusing molecules on a circle with different distributions of the diffusion coefficient in Sec. V B using a finite element discretization over a triangular mesh to discretize the required diffusion operator as in Sec. II B 2. In Sec. V C, we investigate the available range of dynamics when bimolecular reactions are included. Finally, in Sec. V D we look at potential subdiffusive effects when simulating a realistic three-dimensional model of a subsystem of an *E. coli* model. In all examples, the mesoscopic internal states model with variable diffusion coefficients is determined as in Sec. III. With repeatability and reproducibility in mind, the models tested here will be released in the coming version 1.4 of our freely available software URDME [28,63].

A. Stochastic simulation algorithm

The direct simulation method [24] by Gillespie determines the time for the next reaction event and which event that will take place. For spatial problems, the state of the chemical system is a random variable $\mathbf{Y} \in \mathbb{N}^{JKL}$ and is defined by the number of molecules of each species in the internal states in each voxel. The simulation method of choice is then the next subvolume method (NSM) [25]. The probabilities for the events are given by the coefficients in $\mathbf{\Lambda} \otimes \mathbf{T}$ (diffusion), $\mathbf{A}$ (change of internal state), and the reaction propensities in $\mathbf{f}$. The change of internal state in a voxel has the form of a monomolecular reaction.

The NSM algorithm becomes time consuming with multiple internal states since many events simply change the internal states without advancing the observable dynamics. A parallel version suitable for modern multicore computers was developed in [64] which is effective in dealing with events taking place *within* spatial subdomains rather than between them. We remark that introducing the internal states is a way of simulating a system with a random, predetermined diffusion coefficient $\gamma(\mathbf{x}, t)$. Simulation of such a system without internal states requires a special, more complicated version of Gillespie's algorithm to handle time dependent coefficients [65].

TABLE I. Estimated values of subdiffusive constant α for different values of ϕ in Fig. 3(a).

ϕ	0.05	0.10	0.15	0.20	0.25	0.30	0.35	0.40
α	0.84	0.85	0.80	0.75	0.76	0.75	0.69	0.59

B. Pure subdiffusion

There is experimental evidence that the diffusive transport of molecules in cells is sometimes anomalous [6,11,45] with a MSD as in (1). The reason for the subdiffusion may be crowding effects by other molecules and the process is then nonergodic with a memory (see, e.g., [42,66]).

The macroscopic observable $\mathbf{U}(\mathbf{x}, t) \in \mathbb{R}^L$, e.g., the concentrations of the chemical species, satisfies a diffusion equation with a fractional time derivative [45]

$$\frac{\partial \mathbf{U}}{\partial t} = \frac{\partial^{1-\alpha}}{\partial t^{1-\alpha}} (\gamma \Delta \mathbf{U}), \tag{76}$$

with $0 < \alpha < 1$ at least in a time interval $t \in [t_0, t_1]$. The fractional derivative is defined according to Riemann-Liouville. The internal state parameters $\boldsymbol{\mu}$ and $\boldsymbol{\theta}$ are given by statistics obtained with the microscopic model in [38].

We compute the MSD (1) of the internal states model in Fig. 4 by coarse graining into 10 states as in Fig. 3(a) following the procedure described in Sec. III B using $\phi = 0.35$ and $\gamma_0 = 0.01$. The geometry is the unit circle and the molecules are released at time $t = 0$ in the center and in the fastest diffusing internal state with $\gamma_{10} = \gamma_0 \theta_{10}$. Since there are no reactions, all transition rates act linearly and the moment equations are closed such that the mean-square displacement can be accurately determined by solving (56) numerically for $\mathbf{p}$ with $L = 1$ and $\mathbf{R} = 1$ for the probability to be in voxel i. Then, the MSD in (1) is $\langle \|\mathbf{x}(t)\|_2^2 \rangle = \sum_i p_i(t) \|\mathbf{x}_i\|_2^2$ where $\mathbf{x}_i$ is the center of voxel i.

The initial diffusion rate is $\gamma_0 \theta_{10}$ and, as $t \to \infty$, γ converges to $\bar{\gamma}$. The region in-between these two limits is where the subdiffusive behavior is observed, and where $\alpha < 1$ in (1) and (76). Initially and for large t, $\alpha = 1$ and we have ordinary diffusion. By scaling the internal transfer matrix $\mathbf{A}$ with a different κ_0 in (23), this region (indicated by the comparison slope) can be varied accordingly (see Fig. 4), where the same α is obtained with two different values of κ_0. Recall that κ_0 models the speed of diffusion of the obstacles and for an accurate description their average diffusion speed should be known.

The α parameter in the MSD is determined in Table I for different fractions of occupied volume ϕ in Fig. 3(a). These values are obtained by least squares fitting within a window of time in the same manner as in Fig. 4 and are therefore subject to some degree of uncertainty. The trend is that the more crowding with higher ϕ, the lower α is.

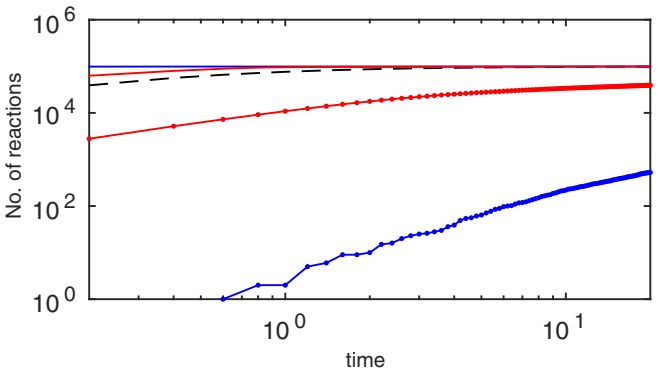

FIG. 5. Results of the bimolecular reaction in (77) presented as the time history of the number of resulting molecules C. The *solid colored* lines represent simulations with H_{ij} in the different cases, from bottom to top: case 1 (blue with dots), case 2 (red with dots), case 3 (smooth red), and case 4 (smooth blue), respectively. The *dashed* line is the pure diffusion case with k_0 as the single rate.

C. Bimolecular annihilation

Consider two species A and B undergoing the single transition

$$A_i + B_j \to C, \tag{77}$$

with A in the internal state i and B in j and with an arbitrary internal state for C. Let the rate for this transition be H_{ij}, $i, j = 1, \ldots, K$. Then, the reaction propensity is $H_{ij}a_i b_j$ where a_i and b_j are the copy numbers of A_i and B_j. Given an arbitrary non-negative rate matrix $\mathbf{H}$, a steady state probability distribution $\mathbf{p}_{A\infty}$ of the internal states for both A and B, and a target rate constant k_0, we can always scale $\mathbf{H}$ such that the mean rate agrees with the target at the steady state

$$k_0 = \mathbf{p}_{A\infty}^T \mathbf{H} \mathbf{p}_{A\infty}. \tag{78}$$

There is potentially great freedom in selecting the rate parameters subject to a scaling. Note that when H_{ij} is independent of i and j and $\mathbf{H} = k_0 \mathbf{e}_L \mathbf{e}_L^T$, the internal states model agrees with the standard model using a single target rate k_0. The diffusion in the internal states is as in the previous example.

We release A and B molecules at time $t = 0$, 10^5 of each species, in 10 internal states uniformly in space in the unit disk with all in the fastest (the 10th) diffusing state. Four different cases of rate parameters are defined as follows:

(1) $H_{1,1} = 1$ and 0 otherwise.
(2) $H_{ij} = (11 - i)(11 - j)$.
(3) $H_{ij} = ij$.
(4) $H_{10,10} = 1$ and 0 otherwise.

Then, the parameters are rescaled such that $\mathbf{H}$ satisfies (78) with $k_0 = 10^{-4}$. In cases 1 and 4, two molecules A and B react only when they both are in the same voxel and in the same internal state. The reaction rate decreases or increases with the diffusion in cases 2 and 3. The combined effect of internal states and reactions is modeled by $\mathbf{H}$ corresponding to $\mathbf{g} \otimes \mathbf{f}$ in (43).

The result obtained from a single realization of the system with URDME, visualized as the number of resulting C molecules, is displayed in Fig. 5. The diffusion data are from Fig. 3(a) at $\phi = 0.2$. The extreme cases 1 and 4 where a single rate in $\mathbf{H}$ is nonzero are clearly identifiable, as are the two intermediate cases 2 and 3. The single state model is found in the middle of all of these cases. Different choices of reaction rates yield a range of different behavior. The idea that there is a freedom in selecting the rate parameters opens up for advanced coarse-graining methods.

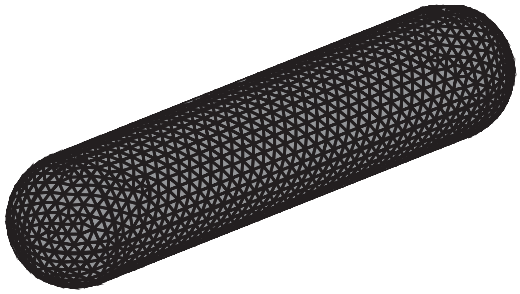

FIG. 6. A discretized model of an *E. coli* bacterium.

While there are different procedures to derive the diffusion rates in the internal states in $\mathbf{A}$ in Sec. III D, there is little theory or data to compute the reaction rates in different internal states in $\mathbf{H}$. If data from detailed simulations of reactions based on, e.g., analytic and simulation results in the diffusion-limited regime [2,67,68], or computational methods based on data from Brownian dynamics [39,40] or molecular dynamics [69] simulations, these data could determine H_{ij}. Here, only examples of rate parameters are tested to see the effect of different transitions between the internal states in the reactions.

D. Min oscillations in *E. coli*

As a more involved example in three space dimensions, we take the model from [70] of the Min system in the *E. coli* bacterium. The geometry is rod shaped with length 3.5 μm, diameter 1 μm, and discretized using 9761 tetrahedra (see Fig. 6). MinD proteins oscillate from pole to pole in the cell with a low concentration in the middle. These oscillations help the cell locate its middle before cell division [71]. The five reactions, five species, and reaction parameters from [70] are found in Table II. Two of the species, MinDmem and MinDE, are attached to the membrane and only diffuse there. The other three species diffuse freely in the cytosol, where the effective diffusion constant is $\gamma_0 = 2.5\ \mu\text{m}^2/\text{s}$ in [70]. Since the inside of an *E. coli* is a highly crowded environment (cf. Fig. 1), it is

TABLE II. The chemical reactions of the Min system. The constants take the values $k_d = 0.0125\ \mu\text{m}^{-1}\,\text{s}^{-1}$, $k_{dD} = 9 \times 10^6\ \text{M}^{-1}\,\text{s}^{-1}$ (here scaled by an additional factor of 1.65 in the numerical experiments), $k_{de} = 5.56 \times 10^7\ \text{M}^{-1}\,\text{s}^{-1}$, $k_e = 0.7\ \text{s}^{-1}$, and $k_p = 0.5\ \text{s}^{-1}$.

$\text{MinDcytATP} \xrightarrow{k_d} \text{MinDmem}$
$\text{MinDcytATP} + \text{MinDmem} \xrightarrow{k_{dD}} 2\text{MinDmem}$
$\text{MinE+MinDmem} \xrightarrow{k_{de}} \text{MinDE}$
$\text{MinDE} \xrightarrow{k_e} \text{MinDcytADP} + \text{MinE}$
$\text{MinDcytADP} \xrightarrow{k_p} \text{MinDcytATP}$

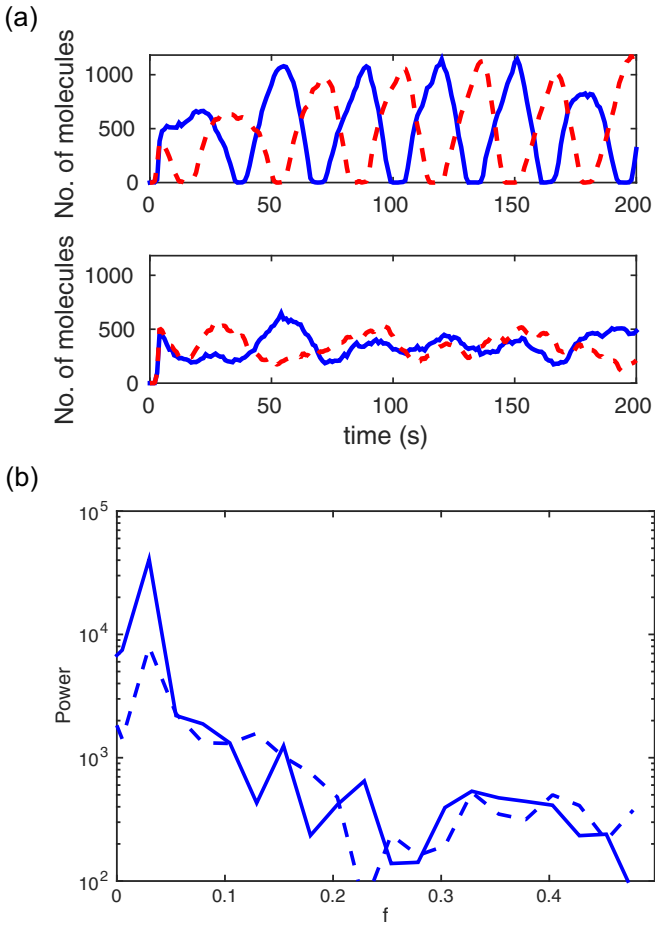

FIG. 7. Two realizations of MinD oscillations in the membrane of an *E. coli* bacterium. (a) The number of MinD molecules in the leftmost (dashed red) and rightmost (solid blue) quarters of the bacterium, respectively. Top: ordinary diffusion without internal states. Bottom: our coarse-grained subdiffusion model. (b) The Fourier power spectrum of the pole oscillations of the two models: ordinary diffusion (solid) and coarse-grained subdiffusion (dashed).

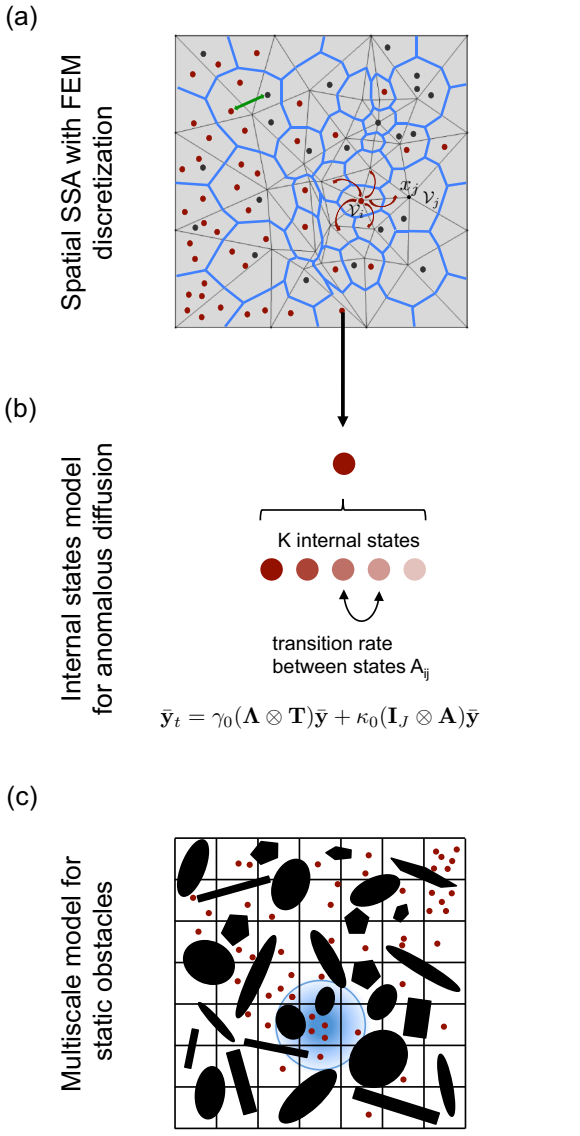

FIG. 8. Summary of the method. (a) A triangulation (gray edges) between the nodes $\mathbf{x}_j$ defines the primal mesh and the dual mesh (blue boundaries) which form the voxels $\mathcal{V}_j$. Red and black tracer molecules diffuse (red arrows) between voxels. They react with each other (green arrow) when they are located in the same voxel. (b) The molecules in a voxel are in K internal states ($K = 5$ here). In the equation without chemical reactions for the mean values $\bar{\mathbf{y}}$ of the number of molecules in each state in every voxel, γ_0 is the free diffusion coefficient, $\mathbf{\Lambda}$ is the matrix of jump coefficients between the voxels given by a finite element discretization, $\mathbf{T}$ scales the hindered diffusion due to crowding in the K internal states, $1/\kappa_0$ determines the time scale of the internal jumps, and $\mathbf{A}$ is the matrix of jump coefficients between the internal states in a voxel. (c) The jump rates between the internal states in $\mathbf{A}$ are determined by computing the mean first exit time from the blue circle for a red tracer molecule with black obstacle molecules. Statistics is collected for many different obstacle configurations. Sampling from this distribution means that the tracer molecule is experiencing different crowder densities and consequently changes its internal state. *Summary:* Our approach focuses on coupling the internal states model (b), which has previously been used to simulate anomalous diffusion, to the explicit description of crowder molecules by coarse graining the microscopic information to the mesoscopic level (c).

of interest to investigate the incorporation of subdiffusion due to crowding and reaction rates depending on the internal state in the mesoscopic model.

As a proof of concept and in order to demonstrate the possibilities here, we scaled the critical binding reaction rate k_{dD} by a factor 1.65, thus bringing the kinetics into a more sensitive regime compared to the original rate. The normally diffusing model then displays stable oscillations of the Min protein in the membrane (see upper left panel in Fig. 7).

As in the previous experiments, we employ 10 internal states obtained from coarse graining with data from Fig. 3(a) at $\phi = 0.2$. For the binding reaction of state i, we multiply k_{dD} by a factor $1 + 0.03i$ meaning that the reactivity increases with faster diffusion. We then rescale the resulting rate as in (78) such that the steady state mean rate agrees with the single state model. To bring in a bias we arbitrarily let all reactions produce products in the fastest diffusing state with $i = 10$ ($A_i + B_j \to C_{10}$, $\forall\, i, j$ where $1 \leqslant i, j \leqslant 10$), thus skewing the distribution over the internal states towards faster diffusion and also faster binding rate. The presence of

subdiffusion and variable reaction rates in this model has a striking effect on the oscillatory behavior. The oscillations are damped considerably (see the lower left panel in Fig. 7). The peak in the power spectrum at about 0.03 Hz in the right panel of Fig. 7 is reduced by more than a factor 6 in the internal state model. With our computational framework, an investigation of the dynamics due to crowding and variable reaction rates is computationally feasible even in nontrivial and quite large examples.

VI. CONCLUSIONS

We have developed a computationally efficient approach to simulate diffusive and subdiffusive transport processes for chemical species on the mesoscopic level taking the explicit description of obstacle sizes and densities into account. Two existing methods are coupled: the internal states model and the coarse graining of a microscopic crowded geometry to the mesoscopic level (see the summary in Fig. 8). Our method is faster than directly simulating microscopic Brownian dynamics and permits more detailed modeling than a standard mesoscopic model with fixed diffusion and reaction coefficients. In other lattice methods for simulation of crowding, only a limited number of molecules can occupy the same voxel in the lattice. Compared to those methods, our method is less heuristic and models the effect of crowding by deriving a distribution of diffusion coefficients from a fine-grain geometry with obstacles of different shape and size.

An observable is the sum of the copy numbers in all internal states. The mean values of the copy numbers of the observables satisfy macroscopic PDEs discretized by a finite element method. The diffusion in the PDE for the observables is not explicitly known unless the mean values of the full mesoscopic system are known.

The crowding model has been implemented in URDME [28,63] and examples in 2D and 3D show the effects of crowding and the modeling of the reactions. The mean-square displacement of a diffusing molecule is computed and the α parameter measuring the deviation from Brownian motion is recorded. Subdiffusive behavior is observed in a time interval after release of the molecule. The reaction propensities vary with the internal state in two examples. The scaling of the reaction coefficients is such that the same steady state is reached but the transient phase differs in the simulations depending on the particular choice of internal representation. This is illustrated in one example. In the other example, a realization of the MinD system without internal states is oscillatory but is irregular with an internal structure in the voxels.

The data for calibration of the internal states are here taken from homogenization of a detailed microscopic model of crowding, but other sources are also possible. One alternative would be to infer the diffusion and reaction rates from the posterior distribution of a Bayesian approach to analysis of experimental data. Another possibility would be to obtain the rates from coarse-graining data from Brownian dynamics or molecular dynamics realizations of diffusion and reactions.

Microscopic and detailed computational methods are very expensive for simulation of biochemical networks and are restricted to smaller subsystems and for short time. Our mesoscopic method including microscopic data offers a fast and accurate approach for larger systems and longer time intervals at a much reduced computational cost.

ACKNOWLEDGMENTS

The development of URDME was partially supported by the Swedish Research Council within the UPMARC Linnaeus center of Excellence (S.E.). S.E. and P.L. would like to thank the Isaac Newton Institute for Mathematical Sciences, Cambridge, for financial support and hospitality during the programme Stochastic Dynamical Systems in Biology: Numerical Methods and Applications where work on this paper was undertaken. This work was supported by EPSRC Grant No. EP/K032208/1.

[1] K. Luby-Phelps, Cytoarchitecture and physical properties of cytoplasm: volume, viscosity, diffusion, intracellular surface area, Int. Rev. Cytol. **192**, 189 (1999).

[2] S. Schnell and T. E. Turner, Reaction kinetics in intracellular environments with macromolecular crowding: Simulations and rate laws, Prog. Biophys. Mol. Biol. **85**, 235 (2004).

[3] P. R. ten Wolde and A. Mugler, Importance of crowding in signaling, genetic, and metabolic networks, Int. Rev. Cell Mol. Biol. **307**, 419 (2014).

[4] B. Grasberger, A. P. Minton, C. DeLisi, and H. Metzger, Interaction between proteins localized in membranes, Proc. Natl. Acad. Sci. USA **83**, 6258 (1986).

[5] S. Jin and A. S. Verkman, Single particle tracking of complex diffusion in membranes: Simulation and detection of barrier, raft, and interaction phenomena, J. Phys. Chem. B **111**, 3625 (2007).

[6] D. Krapf, Mechanisms underlying anomalous diffusion in the membrane, Curr. Topics Membr. **75**, 167 (2015).

[7] O. Medalia, I. Weber, A. S. Frangakis, D. Nicastro, G. Gerisch, and W. Baumeister, Macromolecular architecture in eukaryotic cells visualized by cryoelectron tomography, Science **298**, 1209 (2002).

[8] C. Di Rienzo, V. Piazza, E. Gratton, F. Beltram, and F. Cardarelli, Probing short-range protein Brownian motion in the cytoplasm of living cells, Nat. Commun. **5**, 5891 (2014).

[9] D. S. Banks, C. Tressler, R. D. Peters, F. Höfling, and C. Fradin, Characterizing anomalous diffusion in crowded polymer solutions and gels over five decades in time with variable-lengthscale fluorescence correlation spectroscopy, Soft Matter **12**, 4190 (2016).

[10] M. Galanti, D. Fanelli, A. Maritan, and F. Piazza, Diffusion of tagged particles in a crowded medium, Europhys. Lett. **107**, 20006 (2014).

[11] F. Höfling and T. Franosch, Anomalous transport in the crowded world of biological cells, Rep. Prog. Phys. **76**, 046602 (2013).

[12] D. V. Nicolau Jr., J. F. Hancock, and K. Burrage, Sources of anomalous diffusion on cell membranes: A Monte Carlo study, Biophys. J. **92**, 1975 (2007).
[13] D. Hall and A. P. Minton, Macromolecular crowding: Qualitative and semiquantitative successes, quantitative challenges, Biochim. Biophys. Acta, Proteins Proteomics **1649**, 127 (2003).
[14] T. Ando and J. Skolnick, Crowding and hydrodynamic interactions likely dominate in vivo macromolecular motion, Proc. Natl. Acad. Sci. USA **107**, 18457 (2010).
[15] C. J. Penington, B. D. Hughes, and K. A. Landman, Building macroscale models from microscale probabilistic models: A general probabilistic approach for nonlinear diffusion and multispecies phenomena, Phys. Rev. E **84**, 041120 (2011).
[16] M. J. Saxton, A biological interpretation of transient anomalous subdiffusion. I. Qualitative model, Biophys. J. **92**, 1178 (2007).
[17] S. B. Yuste, L. Acedo, and K. Lindenberg, Reaction front in an $A + B \to C$ reaction-subdiffusion process, Phys. Rev. E **69**, 036126 (2004).
[18] D. J. Kiviet, P. Nghe, N. Walker, S. Boulineau, V. Sunderlikova, and S. J. Tans, Stochasticity of metabolism and growth at the single-cell level, Nature (London) **514**, 376 (2014).
[19] H. H. McAdams and A. Arkin, Stochastic mechanisms in gene expression, Proc. Natl. Acad. Sci. USA **94**, 814 (1997).
[20] J. M. Pedraza and A. van Oudenaarden, Noise propagation in gene networks, Science **307**, 1965 (2005).
[21] V. Shahrezaei and P. S. Swain, The stochastic nature of biochemical networks, Curr. Opin. Biotechnol. **19**, 369 (2008).
[22] P. S. Swain, M. B. Elowitz, and E. D Siggia, Intrinsic and extrinsic contributions to stochasticity in gene expression, Proc. Natl. Acad. Sci. USA **99**, 12795 (2002).
[23] N. G. van Kampen, *Stochastic Processes in Physics and Chemistry*, 2nd ed. (Elsevier, Amsterdam, 2004).
[24] D. T. Gillespie, A general method for numerically simulating the stochastic time evolution of coupled chemical reactions, J. Comput. Phys. **22**, 403 (1976).
[25] J. Elf and M. Ehrenberg, Spontaneous separation of bi-stable biochemical systems into spatial domains of opposite phases, Syst. Biol. IEE Proc. **1**, 230 (2004).
[26] J. Hattne, D. Fange, and J. Elf, Stochastic reaction-diffusion simulation with MesoRD, Bioinformatics **21**, 2923 (2005).
[27] S. A. Isaacson and C. S. Peskin, Incorporating diffusion in complex geometries into stochastic chemical kinetics simulations, SIAM J. Sci. Comput. **28**, 47 (2006).
[28] B. Drawert, S. Engblom, and A. Hellander, URDME: a modular framework for stochastic simulation of reaction-transport processes in complex geometries, BMC Syst. Biol. **6**, 76 (2012).
[29] S. Engblom, L. Ferm, A. Hellander, and P. Lötstedt, Simulation of stochastic reaction-diffusion processes on unstructured meshes, SIAM J. Sci. Comput. **31**, 1774 (2009).
[30] K. Burrage, P. Burrage, A. Leier, and T. Marquez-Lago, A review of stochastic and delay simulation approaches in both time and space in computational cell biology, in *Stochastic Processes, Multiscale Modeling, and Numerical Methods for Computational Cellular Biology*, edited by D. Holcman (Springer, Cham, 2017), pp. 241–261.
[31] S. Engblom, A. Hellander, and P. Lötstedt, Multiscale simulation of stochastic reaction-diffusion networks, in *Stochastic Processes, Multiscale Modeling, and Numerical Methods for Computational Cellular Biology*, edited by D. Holcman (Springer, Cham, 2017), pp. 55–79.
[32] A. Mahmutovic, D. Fange, O. G. Berg, and J. Elf, Lost in presumption: stochastic reactions in spatial models, Nat. Methods **9**, 1163 (2012).
[33] S. Smith and R. Grima, Spatial stochastic intracellular kinetics: A review of modeling approaches, Bull. Math. Biol. (2018), doi: 10.1007/s11538-018-0443-1.
[34] E. Roberts, J. E. Stone, and Z. Luthey-Schulten, Lattice microbes: High-performance stochastic simulation method for the reaction-diffusion master equation, J. Comput. Chem. **34**, 245 (2013).
[35] D. Fanelli and A. J. McKane, Diffusion in a crowded environment, Phys. Rev. E **82**, 021113 (2010).
[36] K. A. Landman and A. E. Fernando, Myopic random walkers and exclusion processes: Single and multispecies, Physica A (Amsterdam) **390**, 3742 (2011).
[37] P. R. Taylor, C. A. Yates, M. J. Simpson, and R. E. Baker, Reconciling transport models across scales: The role of volume exclusion, Phys. Rev. E **92**, 040701 (2015).
[38] L. Meinecke, Multiscale modeling of diffusion in a crowded environment, Bull. Math. Biol. **79**, 2672 (2017).
[39] S. S. Andrews, N. J. Addy, R. Brent, and A. P. Arkin, Detailed simulations of cell biology with Smoldyn 2.1, PLoS Comput. Biol. **6**, e1000705 (2010).
[40] J. S. van Zon and P. R. ten Wolde, Green's-function reaction dynamics: A particle-based approach for simulating biochemical networks in time and space, J. Chem. Phys. **123**, 234910 (2005).
[41] S. Smith and R. Grima, Fast simulation of Brownian dynamics in a crowded environment, J. Chem. Phys. **146**, 024105 (2017).
[42] T. T. Marquez-Lago, A. Leier, and K. Burrage, Anomalous diffusion and multifractional Brownian motion: simulating molecular crowding and physical obstacles in systems biology, IET Syst. Biol. **6**, 134 (2012).
[43] L. Meinecke and M. Eriksson, Excluded volume effects in on- and off-lattice reaction-diffusion models, IET Syst. Biol. **11**, 55 (2017).
[44] E. Barkai, Y. Garini, and R. Metzler, Strange kinetics of single molecules in living cells, Phys. Today **65**(8), 29 (2012).
[45] R. Metzler and J. Klafter, The random walk's guide to anomalous diffusion: a fractional dynamics approach, Phys. Rep. **339**, 1 (2000).
[46] M. S. Mommer and D. Lebiedz, Modeling subdiffusion using reaction diffusion systems, SIAM J. Appl. Math. **70**, 112 (2009).
[47] E. Blanc, S. Engblom, A. Hellander, and P. Lötstedt, Mesoscopic modeling of stochastic reaction-diffusion kinetics in the subdiffusive regime, Multiscale Model. Simul. **14**, 668 (2016).
[48] F. Persson, M. Lindén, C. Unoson, and J. Elf, Extracting intracellular diffusive states and transition rates from single molecule tracking data, Nat. Methods **10**, 265 (2013).
[49] T. Bauer, F. Höfling, T. Munk, E. Frey, and T. Franosch, The localization transition of the two-dimensional Lorentz model, Eur. Phys. J. Special Topics **189**, 103 (2010).
[50] M. Spanner, F. Höfling, S. C. Kapfer, K. R. Mecke, G. E. Schröder-Turk, and T. Franosch, Splitting of the Universality Class of Anomalous Transport in Crowded Media, Phys. Rev. Lett. **116**, 060601 (2016).
[51] B. Øksendal, *Stochastic Differential Equations*, 6th ed. (Springer, Berlin, 2003).

[52] M. D. Gunzburger, C. G. Webster, and G. Zhang, Stochastic finite element methods for partial differential equations with random input data, Acta Numerica **23**, 521 (2014).
[53] P. Lötstedt and L. Meinecke, Simulation of stochastic diffusion via first exit times, J. Comput. Phys. **300**, 862 (2015).
[54] L. Meinecke, S. Engblom, A. Hellander, and P. Lötstedt, Analysis and design of jump coefficients in discrete stochastic diffusion models, SIAM J. Sci. Comput. **38**, A55 (2016).
[55] C. Gadgil, C. H. Lee, and H. G. Othmer, A stochastic analysis of first-order reaction networks, Bull. Math. Biol. **67**, 901 (2005).
[56] S. Smith, C. Cianci, and R. Grima, Macromolecular crowding directs the motion of small molecules inside cells, J. R. Soc. Interface **14**, 20170047 (2017).
[57] J. Szymanski and M. Weiss, Elucidating the Origin of Anomalous Diffusion in Crowded Fluids, Phys. Rev. Lett. **103**, 038102 (2009).
[58] S. C. Weber, A. J. Spakowitz, and J. A. Theriot, Bacterial Chromosomal Loci Move Subdiffusively Through a Visco elastic Cytoplasm, Phys. Rev. Lett. **104**, 238102 (2010).
[59] M. V. Chubynsky and G. W. Slater, Diffusing Diffusivity: A Model for Anomalous, Yet Brownian, Diffusion, Phys. Rev. Lett. **113**, 098302 (2014).
[60] A. V. Chechkin, F. Seno, R. Metzler, and I. M. Sokolov, Brownian Yet Non-Gaussian Diffusion: from Superstatistics to Subordination of Diffusing Diffusivities, Phys. Rev. X **7**, 021002 (2017).
[61] Ralph C. Smith, *Uncertainty Quantification: Theory, Implementation, and Applications*, Vol. 12 (SIAM, Philadelphia, 2013).
[62] T. Jahnke and W. Huisinga, Solving the chemical master equation for monomolecular reaction systems analytically, J. Math. Biol. **54**, 1 (2007).
[63] S. Engblom *et al.*, URDME: Unstructured Reaction-Diffusion Master Equation (multiple versions exist). Available at www.urdme.org.
[64] J. Lindén, P. Bauer, S. Engblom, and B. Jonsson, Exposing inter-process information for efficient parallel discrete event simulation of spatial stochastic systems, in *Proceedings of the 2017 ACM SIGSIM Conference on Principles of Advanced Discrete Simulation (SIGSIM-PADS'17)* (ACM, New York, 2017), pp. 53–64.
[65] M. A. Gibson and J. Bruck, Efficient exact stochastic simulation of chemical systems with many species and many channels, J. Phys. Chem. **104**, 1876 (2000).
[66] R. Hilfer and L. Anton, Fractional master equations and fractal time random walks, Phys. Rev. E **51**, R848 (1995).
[67] R. Grima and S. Schnell, A systematic investigation of the rate laws valid in intracellular environments, Biophys. Chem. **124**, 1 (2006).
[68] B. I. Henry, T. A. M. Langlands, and S. L. Wearne, Anomalous diffusion with linear reaction dynamics: From continuous time random walks to fractional reaction-diffusion equations, Phys. Rev. E **74**, 031116 (2006).
[69] S. Pronk, S. Páll, R. Schulz, P. Larsson, P. Bjelkmar, R. Apostolov, M. R. Shirts, J. C. Smith, P. M. Kasson, D. van der Spoel, B. Hess, and E. Lindahl, GROMACS 4.5: a high-throughput and highly parallel open source molecular simulation toolkit, Bioinformatics **29**, 845 (2013).
[70] D. Fange and J. Elf, Noise induced Min phenotypes in *E. coli*, PLoS Comput. Biol. **2**, e80 (2006).
[71] K. Kruse, A dynamic model for determining the middle of *Escherichia coli*, Biophys. J. **82**, 618 (2002).